HHS Public Access

Author manuscript

NMR Biomed. Author manuscript; available in PMC 2022 March 14.

Published in final edited form as:

NMR Biomed. 2022 January ; 35(1): e4613. doi:10.1002/nbm.4613.

High fidelity fiber orientation density functions from fiber ball imaging

Hunter G. Moss[1,2], **Jens H. Jensen**[1,2,3]

[1]Center for Biomedical Imaging, Medical University of South Carolina, Charleston, South Carolina

[2]Department of Neuroscience, Medical University of South Carolina, Charleston, South Carolina

[3]Department of Radiology and Radiological Science, Medical University of South Carolina, Charleston, South Carolina

Abstract

The fiber orientation density function (fODF) in white matter is a primary physical quantity that can be estimated with diffusion MRI. It has often been employed for fiber tracking and microstructural modeling. Requirements for the construction of high fidelity fODFs, in the sense of having good angular resolution, adequate data to avoid sampling errors, and minimal noise artifacts, are described for fODFs calculated with fiber ball imaging. A criterion is formulated for the number of diffusion encoding directions needed to achieve a given angular resolution. The advantages of using large *b*-values (≥6000 s/mm^2) are also discussed. For the direct comparison of different fODFs, a method is developed for defining a local frame of reference tied to each voxel's individual axonal structure. The Matusita anisotropy axonal is proposed as a scalar fODF measure for quantifying angular variability. Experimental results, obtained at 3 T from human volunteers, are used as illustrations.

Keywords

angular resolution; diffusion MRI; fiber ball imaging; fiber orientation density function; high *b*-value; white matter

1 | INTRODUCTION

The geometrical arrangement of axon orientations inside a small region of white matter is described by the fiber orientation density (or distribution) function (fODF).[1–3] Estimation of the fODF for individual imaging voxels is one of the more remarkable abilities of diffusion MRI (dMRI), providing a unique picture of the intricate details of brain tissue cytoarchitecture. Heretofore, fODFs have mainly been applied to support fiber tractography[4]

Correspondence Jens H. Jensen, Department of Neuroscience, Medical University of South Carolina, Basic Science Building, MSC 510, South Carolina. jense@musc.edu.

DATA AVAILABILITY STATEMENT

Research data are not shared.

SUPPORTING INFORMATION

Additional supporting information may be found in the online version of the article at the publisher's website.

and microstructural modeling.[5–8] In both cases, the fODF is essentially regarded as an input for the calculation of other physical quantities. However, as technical innovations lead to improving methods for measuring fODFs, it becomes natural to explore whether the fODF could itself be valuable as a direct window into cytoarchitectural changes associated with brain development, aging, and disease. Specifically, several open questions spring to mind. How variable are fODFs from a given brain region across individuals? How do fODFs change with age? How are fODFs affected by stroke, epilepsy, and Alzheimer's disease?

To appreciate the information that the fODF provides, it is important to have a clear understanding of its physical meaning. One way to explain this is to imagine picking a water molecule at random from within the axoplasm of a given voxel, as illustrated in Figure 1. Note that water within the myelin and extra-axonal water are not included. Then the fODF for this voxel is simply the probability density, $F(\mathrm{u})$, of the axon that contains the water molecule being oriented in a direction u. If the axon is curved, then it is the orientation in the vicinity of the water molecule that counts. Thus the fODF is entirely determined by axon morphometry and could, at least in principle, be calculated from three-dimensional white matter histology. One caveat, however, is that it is not definitively known whether the fODF, as estimated with dMRI, includes both myelinated and unmyelinated axons, but some evidence does indicate that myelinated axons give the predominant contribution to the fODF for typical dMRI data acquisitions.[9] A more precise mathematical definition of the fODF is given in Appendix A.

In order to obtain and utilize high fidelity fODF maps that support meaningful comparison of fODF structure across voxels and subjects, several issues need to be addressed. First, it is important that the angular resolution of the fODF maps be known so they can be properly interpreted. Second, criteria for choosing the number of diffusion encoding directions and the diffusion weighting are needed to avoid sampling errors and noise artifacts. Excessive sampling errors and signal noise degrade fODF maps and obscure the finer details of fODF structure. Third, fODFs should be plotted consistently in a local frame of reference that is determined by the fODF structure itself rather than in a global frame as is typically done. Global frames (eg the laboratory frame) are necessary for fiber tracking, but they confound the comparison of fODF structure since the appearance of fODF maps in global coordinates depends on both structure and spatial orientation. By using a local frame of reference, the effect of spatial orientation can be removed. Finally, quantitative methods for comparing fODFs across voxels and subjects are required to fully exploit the information they provide.

The goal of this paper is to address these issues in the context of fiber ball imaging (FBI), which is one approach for constructing fODFs.[6,9,10] An advantage of FBI is that fODFs are calculated by simply applying a linear transform to the dMRI signal data from a single b-value shell without the need to introduce a global response function or numerical regularization. Nevertheless, much of the methodology proposed here is also applicable to other fODF approaches. Examples of high fidelity fODFs constructed from dMRI data obtained at 3 T are used to demonstrate the quality that can be achieved for various choices of imaging parameters.

2 | METHODS

2.1 | Fiber ball imaging

The core equation that underpins FBI is that the fODF is approximately given by

$$F(\mathbf{u}) = \frac{k}{2\bar{S}}\tilde{\boldsymbol{T}}_{\mathrm{F}}^{-1}\left\{S\right\}(\mathbf{u}, bD_0), \tag{1}$$

where S is the dMRI signal as a function of diffusion encoding direction u for a given b-value shell, $\tilde{\mathbf{T}}_{\mathrm{F}}^{-1}\left\{f\right\}$ is the inverse generalized Funk transform, $\bar{S}$ is the signal averaged over all diffusion encoding directions, b is the b-value, D_0 is a chosen diffusivity scale, and k is a normalization constant.[9,10] The generalized Funk transform and its inverse are both linear operators, and they are discussed in detail in Appendix B. Equation 1 presumes that the dMRI signal has the antipodal symmetry $S(-u) = S(u)$, which is required for the inverse generalized Funk transform to exist. This is typically true for dMRI data to a good approximation,[11] and in practice any departures from antipodal symmetry are easily removed in the preprocessing. In this work, we choose the normalization constant k so that

$$\int d\Omega_{\mathrm{u}} F(\mathbf{u}) = 1\,. \tag{2}$$

The derivation of Equation 1 assumes that axons can be idealized as thin, straight, impermeable cylinders and that the b-value is sufficiently high to suppress the signal from extra-axonal water relative to the signal from water in the more restricted intra-axonal compartment. Additional requirements and support for the validity of Equation 1 are discussed in prior work.[6,9,10,12] In particular, the observed decrease of the direction-averaged dMRI signal as $1/\sqrt{b}$ for high b-values provides strong corroboration of the thin cylinder approximation.[9,12–14] Typically, the b-value should be about 4000 s/mm^2 or larger for healthy, adult human brain when using 3 T scanners. Equation 1 is only applicable to white matter and likely quantifies the angular density of mainly myelinated axons.

Because of antipodal symmetry, the dMRI signal can be expanded solely in terms of even degree spherical harmonics as

$$S(\mathbf{u}) = S_0 \sum_{l=0}^{\infty} \sum_{m=-2l}^{2l} a_{2l}^m Y_{2l}^m(\theta, \varphi), \tag{3}$$

where (θ, φ) are the spherical angles for the direction vector u, $\mathrm{Y}_{\mathrm{l}}^{\mathrm{m}}(\theta, \varphi)$ is the spherical harmonic of degree l and order m, a_{2l}^m are the expansion coefficients, and S_0 is the signal when the b-value is set to zero. From Equations B5, 1, and 3, along with linearity of the generalized Funk transform, one then sees that

$$F(\mathbf{u}) = \sum_{l=0}^{\infty} \sum_{m=-2l}^{2l} c_{2l}^m Y_{2l}^m(\theta, \varphi), \tag{4}$$

where

$$c_{2l}^{m} = \frac{k S_0 a_{21}^{m}}{2\bar{S}\tilde{\lambda}_{2l}(bD_0)} \tag{5}$$

with $\tilde{\lambda}_{2l}(bD_0)$ being an eigenvalue for the generalized Funk transform (see Appendix B for details). Equations 2–5, B6, and B10 imply

$$k = \frac{\tilde{\lambda}_0(bD_0)}{2\pi} = \mathrm{erf}\sqrt{bD_0}, \tag{6}$$

where erf(x) is the error function.

The diffusivity scale D_0 is an adjustable parameter, but should be chosen so that $D_0 \geq D_a$, where D_a is the intrinsic intra-axonal diffusivity.[10] For D_0, standard choices are either $D_0 = D_a$, which requires that a reliable estimate for D_a be available, $D_0 = D_f$, where D_f is the diffusivity of free water, or $D_0 = \infty$. For $D_0 = \infty$, the inverse generalized Funk transform reduces to the inverse of the classical Funk transform, as follows from Equation B3. For finite D_0, the estimate of the fODF provided by Equation 1 becomes more accurate but also more sensitive to signal noise.[9,10] However, for a fixed signal-to-noise ratio (SNR), the impact of the choice of D_0 decreases as the b-value is increased. At a body temperature of 37 C, we have $D_f \approx 3.0$ μm^2/ms.[15] The choice $D_0 = D_a$ should theoretically give the best accuracy, but D_a is difficult to measure with single diffusion encoding MRI.[16] Thus the other choices may often be more convenient.

In white matter, $D_a \approx 2.25$ μm^2/ms.[17] Since FBI requires b≥ 4000 s/mm^2, one would usually have $bD_0 \geq 9$. This implies

$$0.99998 \approx \mathrm{erf}(3) \leq k \leq \mathrm{erf}(\infty) = 1\,. \tag{7}$$

Therefore, in all cases of interest, the normalization constant k is very close to one.

2.2 | Angular resolution

For an experiment in which dMRI data are acquired on the b-value shell for N distinct diffusion encoding directions, only a finite number of terms in the signal expansion of Equation 3 can be accurately estimated. Therefore, this expansion is typically truncated as

$$S(\mathbf{u}) = S_0 \sum_{l=0}^{L} \sum_{m=-2l}^{2l} a_{2l}^{m} Y_{2l}^{m}(\theta, \varphi), \tag{8}$$

where $2L$ is the maximum degree of the retained spherical harmonics. Because the signal is a real function, the expansion coefficients must have the property

$$\bar{a_{2l}^{m}} = (-1)^{m} a_{2l}^{m\,*} \tag{9}$$

with the asterisk indicating complex conjugation. This implies that, for each value of l in Equation 8, there are $4l+1$ independent parameters to be calculated from the data. As the number of diffusion encoding directions should equal or exceed the number of independent parameters, one finds that $N \geq (L+1)(2L+1) \equiv N_{2L}$. Here we have defined N_{2L} as the total number of independent parameters for the signal's spherical harmonic expansion, which sets the minimum number of diffusion encoding directions needed to uniquely determine the expansion coefficients up to a degree $2L$.

With FBI, the fODF is a linear transform of the signal. Hence, the spherical harmonic expansion of Equation 4 must be similarly truncated to

$$F(\mathbf{u}) = \sum_{l=0}^{L} \sum_{m=-2l}^{2l} c_{2l}^{m} Y_{2l}^{m}(\theta, \varphi)\,. \tag{10}$$

This restriction on the number terms that may be included in the fODF's spherical harmonic representation means that its angular resolution, as estimated with FBI, is limited. To find a quantitative connection between angular resolution and the maximum degree $2L$, we consider an fODF that is concentrated in the direction defined by $\theta = 0$. The estimated fODF obtained from Equations 1 and 10 is

$$F_{\mathrm{PSF}}(\mathbf{u}) = \frac{1}{4\pi} \sum_{1=0}^{L} (4l+1) \frac{\tilde{\lambda}_{2l}(bD_a)}{\tilde{\lambda}_{2l}(bD_0)} P_{2l}(\cos\theta), \tag{11}$$

where $P_1(x)$ is the Legendre polynomial of degree l; Equation 11 corresponds to the point spread function (PSF) for the degree $2L$. This PSF is peaked near $\theta = 0$ and $\theta = \pi$, as illustrated by Figure S2 of the Supporting Information. The angular resolution for a degree $2L$ may be defined as the full width at half the maximum of this central PSF peak. From Equation 11, we see that the angular resolution, α_{2L}, can be determined from

$$2\sum_{I=0}^{L} (4I+1) \frac{\tilde{\lambda}_{2l}(bD_a)}{\lambda_{2l}(bD_0)} P_{2l}\left(\cos\frac{\alpha_{2L}}{2}\right) = \sum_{l=0}^{L} (4I+1) \frac{\tilde{\lambda}_{2l}(bD_a)}{\tilde{\lambda}_{2l}(bD_0)}\,. \tag{12}$$

Numerical solutions to Equation 12 are given in Table 1 for $D_0 = D_a$ and $L = 1$ to 10. Note that in this case the angular resolution is independent of both D_a and b. One can also show that $D_0 = D_a$ gives the best possible angular resolution for a given value of L and that this is well approximated by

$$\alpha_{2L} \approx \frac{3.13}{\sqrt{N_{2L}-1}}\,. \tag{13}$$

Plots of α_{2L} as a function of the b-value for D_0 equal to D_a, 3 $\mu m^2/ms$ (ie D_f), and ∞ are shown in Figure 2 with $L = 3$ to 6. While the angular resolution for $D_0 = 3$ $\mu m^2/ms$ is close to that for $D_0 = D_a$, setting $D_0 = \infty$ results in a substantially poorer resolution, especially for the lower b-values. For this reason, the choice $D_0 = \infty$ is not recommended for high fidelity

fODFs. These plots are calculated using D_a= 2.25 μm^2/ms, which is a typical value for healthy white matter.[17]

2.3 | Sampling errors

If the number of diffusion encoding directions is set to the strict minimum value of N_{2L}, then the computed fODFs will be prone to sampling errors due to aliasing, as is familiar in the context of Fourier transforms but also applies to spherical harmonic expansions.[18,19] Moreover, any aliasing errors that occur in the spherical harmonic expansion for the dMRI signal are amplified in the fODF through application of the inverse generalized Funk transform of Equation 1, which tends to increase the relative contribution of the higher degree terms. This is of particular importance in fODFs with sharp features since large angular frequencies are most susceptible to aliasing foldover (or wraparound) artifacts.

A standard procedure for reducing aliasing artifacts is to oversample the data. This creates a "guard band" in the frequency spectrum that serves to limit penetration of foldover artifacts into the calculated spectral range. For example, in MRI, the signal in the frequency encoding direction is routinely oversampled by a factor of 2 in order to decrease aliasing.[20,21] The analogous degree of oversampling for spherical harmonics with antipodal symmetry would be to use $N_{4L} \approx 4N_{2L}$ diffusion encoding directions. In some contexts, using even more than $4N_{2L}$ samples has been recommended to obtain reliable estimates of spherical harmonic expansion coefficients.[22] While this would often be impractical for dMRI, oversampling by factors of 2 to 3 is feasible and can significantly attenuate sampling errors in fODF estimation.

Taking N = 300 as a practical upper limit on the number of diffusion encoding directions that can be conveniently obtained for in vivo human dMRI, oversampling by a factor of 3 implies $N_{2L} \lesssim 100$. From Table 1, we see that this leads to $2L \leq 12$ and an angular resolution of no better than about 18.9°. While this may seem coarse, it is similar to the extent of axonal fanning found from histology in the corpus callosum,[23] which has a relatively high diffusion anisotropy,[24] and this resolution may therefore be sufficient to depict the main features of many fODFs.

2.4 | Diffusion weighting

In order to obtain high fidelity fODFs, a proper choice of b-value is essential. As previously mentioned, FBI generally requires b-values of about 4000 s/mm^2 or higher in order to suppress the dMRI signal from extra-axonal water relative to that from intra-axonal water. The hallmark of a sufficiently high b-value is a scaling of the direction-averaged signal as $1/\sqrt{b}$, which is the experimental signature of diffusing spins confined to thin cylinders (eg axons). While 4000 s/mm^2 is an approximate threshold at which this behavior becomes apparent, the ideal $1/\sqrt{b}$ power law decay is realized more accurately for b-values of 6000 s/mm^2 and higher.[9,12,14] Therefore, if high fidelity fODFs are desired, b-values of 6000 s/mm^2 and above can be recommended for human dMRI at 3 T.

However, power law scaling of the direction-averaged signal eventually breaks down when the b-value is too high, at which point FBI is no longer a valid method. This is because

the diffusion wave vector becomes large enough that the finite diameters of the axons begin to affect the dMRI signal substantially.[25] From the theory of q-space imaging,[26] the quantitative criterion for this is (in the short gradient pulse approximation)

$$d < \frac{1}{2q} = \pi\sqrt{\frac{\Delta}{b}}, \tag{14}$$

where d is the axon diameter, Δ is the diffusion time, and $q = \sqrt{b/\left(4\pi^2\Delta\right)}$ is the wave vector amplitude. Equation 14 implies an upper bound on the diffusion weighting of

$$b < \frac{\pi^2\Delta}{d^2}. \tag{15}$$

For d = 4 μm and Δ= 30 ms, this gives b < 18 500 s/mm^2. Departures from the $1/\sqrt{b}$ scaling have indeed been observed for b-values exceeding this limit[25]. For small axons, with $d < \sqrt{D_a\delta}$, where δ is the gradient pulse duration, the short gradient pulse approximation may not apply, but in [11] this case motional narrowing makes detecting the effect of a finite axon diameter even more difficult than indicated by Equation 15.

Diffusion weighting also has a significant impact on noise artifacts for fODFs estimated with FBI. From the FBI noise theory derived by Jensen and coworkers,[10] the noise variance of spherical harmonic expansion coefficient c_{2l}^m scales with the b-value approximately as

$$\mathrm{var}(c_{2l}^m) \propto b\left[\frac{g_0(bD_0)}{g_{2l}(bD_0)}\right]^2 \approx b\exp\left[\frac{I(2l+1)}{bD_0}\right], \tag{16}$$

where we have used the approximation of Equation B9. This is a decreasing function of the b-value as long as

$$b < \frac{I(2l+1)}{D_0}. \tag{17}$$

With $l = 4$ and $D_0 = 3$ μm^2/ms, the inequality of Equation 17 yields $b < 12\,000$ s/mm^2. Thus, for $D_0 \leq 3$ μm^2/ms, the noise variance of higher degree harmonics decreases up to rather large b-values. Since the higher degree harmonics contribute to the fine structure of the fODFs, using the largest feasible b-value can improve fidelity. An important caveat, however, is that the derivation of Equation 16 assumes that the echo time (T_E) is fixed and the SNR is sufficiently high that rectified noise bias can be neglected. In practice, a larger b-value will typically necessitate a somewhat longer T_E, resulting in stronger T_2 signal decay and lower SNR. Nonetheless, a rule of thumb for achieving high fidelity fODFs with FBI on 3 T clinical scanners is to use the largest b-value for which the SNR is adequate to avoid sizable rectified noise bias. On clinical systems equipped with strong field gradients (ie $\gtrsim$ 80 mT/m), the b-value range of 6000 to 12 000 s/mm^2 would often be appropriate for voxel volumes of 20 to 30 mm^3.

2.5 | Local reference frame

If a global reference frame is used to represent the fODFs, it is difficult to compare the fine structure of two fODFs with different spatial orientations. This problem can be ameliorated by employing a local frame based solely on each fODF's individual structure. To define a local reference frame for an fODF, we first introduce the symmetric tensor

$$\mathbf{A} \equiv \int d\Omega_{\mathrm{u}} F(\mathbf{u}) \mathbf{u}\mathbf{u}^{\top}. \tag{18}$$

This tensor has three orthogonal eigenvectors ($\mathbf{e}_1$, $\mathbf{e}_2$, $\mathbf{e}_3$) along with three associated eigenvalues (λ_1, λ_2, λ_3). We assume that these are ordered so that $\lambda_1 \geq \lambda_2 \geq \lambda_3$ and that the eigenvectors are normalized to unit magnitude. The tensor **A** is equal to the diffusion tensor for the intra-axonal compartment divided by D_{a} and is sometimes referred to as the orientation or scatter matrix.[6,27] The three eigenvectors of **A** provide the basis for a local reference frame for the fODF that is independent of the global reference frame. However, there are sign ambiguities in the definition of the eigenvectors, since an eigenvector multiplied by minus one is still an eigenvector with the same eigenvalue. Thus, three conditions on the eigenvectors must be imposed to uniquely specify the reference frame. For the first condition, we choose

$$\int d\Omega_{\mathbf{u}} F(\mathbf{u})(\mathbf{u}\cdot\mathbf{e}_2)[\mathbf{u}\cdot(\mathbf{e}_2\times\mathbf{e}_3)]^3 \geq 0. \tag{19}$$

The integral on the left-hand side of Equation 19 is an odd function of $\mathbf{e}_3$ but an even function of $\mathbf{e}_2$. Therefore, it fixes the sign of $\mathbf{e}_3$ except for the special case in which the integral exactly vanishes (which is unlikely to occur with real data). The integrand in Equation 19 has a function depending on the fourth power of the direction u, rather than the second power as in Equation 18, in order to have information independent of the tensor A. Similarly, our second condition is

$$\int d\Omega_{\mathbf{u}} F(\mathbf{u})(\mathbf{u}\cdot\mathbf{e}_3)[\mathbf{u}\cdot(\mathbf{e}_2\times\mathbf{e}_3)]^3 \geq 0, \tag{20}$$

which fixes the sign of $\mathbf{e}_2$. The final condition is

$$\mathbf{e}_1\cdot(\mathbf{e}_2\times\mathbf{e}_3) > 0 \tag{21}$$

and fixes the sign of $\mathbf{e}_1$. Equation 21 simply means that the eigenvectors define a right-handed Cartesian coordinate system. Alternative conditions to resolve the eigenvector sign ambiguities are possible, but Equations 19–21 are among the simplest.In terms of the spherical harmonic expansion coefficients for the fODF, the tensor A is given explicitly by[6]

$$\mathbf{A} = \frac{1}{c_0^0\sqrt{30}} \begin{pmatrix} \frac{\sqrt{30}}{3}c_0^0 - \frac{\sqrt{6}}{3}c_2^0 + c_2^2 + c_2^{-2} & ic_2^2 - ic_2^{-2} & -c_2^1 + c_2^{-1} \\ ic_2^2 - ic_2^{-2} & \frac{\sqrt{30}}{3}c_0^0 - \frac{\sqrt{6}}{3}c_2^0 - c_2^2 - c_2^{-2} & -ic_2^1 - ic_2^{-1} \\ -c_2^1 + c_2^{-1} & -ic_2^1 - ic_2^{-1} & \frac{\sqrt{30}}{3}c_0^0 + \frac{2\sqrt{6}}{3}c_2^0 \end{pmatrix}. \quad (22)$$

This is automatically a real, symmetric matrix with a unit trace that can be diagonalized for each voxel to find the three local reference frame eigenvectors.

To plot two-dimensional fODF maps, it is convenient to employ local spherical angles defined by

$$\mathbf{u} = \mathbf{e}_1\cos\theta + \mathbf{e}_2\sin\theta\cos\varphi + \mathbf{e}_3\sin\theta\sin\varphi\,. \quad (23)$$

Azimuthal projection coordinates in the xy-plane are then given by $x = r(\theta)\cos\varphi$ and $y = r(\theta)\sin\varphi$ with the function r(θ) specifying the type of azimuthal projection. The choice r(θ) = θ corresponds to an equidistant azimuthal projection, the choice $r(\theta) = 2\sin(\theta/2)$ corresponds to an equal-area azimuthal projection, and the choice $r(\theta) = 2\tan(\theta/2)$ corresponds to a stereographic azimuthal projection.[28] Because of antipodal symmetry, the fODF only need be plotted over the hemisphere defined by $0 \le \theta \le \pi/2$ and $0 \le \varphi \le 2\pi$ in order to have a complete representation. Maps of fODFs will then appear in the xy-plane as disks with a radius of $\pi/2$ for the hemispheric equidistant azimuthal projection (HEAP) $\sqrt{2}$ for hemispheric equal-area azimuthal projection, and 2 for the hemispheric stereographic azimuthal projection. The direction e corresponds to the central point $\theta = 0$ and $\varphi = 0$, the direction $\mathbf{e}_2$ corresponds to the point $\theta = \pi/2$ and $\varphi = 0$, and the direction $\mathbf{e}_3$ corresponds to the point $\theta = \pi/2$ and $\varphi = \pi/2$. In this paper, we employ HEAP maps since they are among the best flat projections of a sphere for minimizing distortion errors.[29,30]

2.6 | Distance measure for fODFs

For quantitative comparison of fODFs, it is useful to employ a distance measure that reflects how similar two fODFs are. The mathematics literature offers many possibilities.[31] A familiar one is the Euclidian distance

$$d_E \equiv \sqrt{\int d\Omega_u [F_1(\mathbf{u}) - F_2(\mathbf{u})]^2}, \quad (24)$$

where $F_1(u)$ and $F_2(u)$ are two fODFs, each expressed in its own local frame of reference. Another attractive choice is the Matusita distance[32]

$$d_{\mathrm{M}} \equiv \sqrt{\int d\Omega_{\mathrm{u}} \left[\sqrt{F_1(\mathbf{u})} - \sqrt{F_2(\mathbf{u})}\right]^2}, \tag{25}$$

which has often been used in the context of probability densities. A potential advantage of the Matusita distance is that it is less strongly dominated by the largest fODF peaks than is the Euclidian distance and may thereby be more sensitive to differences in fine structure. In addition, the Matusita distance can never exceed $\sqrt{2}$, while the Euclidian distance is unbounded. The Matusita distance is closely related to the Bhattacharyya and Hellinger distances.[31]

For every type of distance, there is an associated anisotropy measure defined as the distance from an fODF with a constant value across all directions. For the normalization of Equation 2, this constant value is $1/4\pi$. The Matusita anisotropy axonal (MAA) is thus given by

$$\mathrm{MAA} \equiv \frac{1}{\sqrt{2}} \sqrt{\int d\Omega_{\mathrm{u}} \left[\sqrt{F(u)} - \frac{1}{\sqrt{4\pi}}\right]^2}, \tag{26}$$

where we have included a factor of $1/\sqrt{2}$ so that $0 \leq \mathrm{MAA} \leq 1$. An important distinction between anisotropies based on distance measures and the fractional anisotropy of the axonal compartment (FAA) is that the FAA only depends on the spherical expansion coefficients of degrees zero and two,[6] but distance-based anisotropies generally depend on all of the expansion coefficients. For instance, if

$$F(\mathbf{u}) = \frac{1}{\sqrt{4\pi}} Y_0^0(\theta, \varphi) + \frac{7}{18\sqrt{\pi}} Y_4^0(\theta, \varphi), \tag{27}$$

then FAA is zero but $\mathrm{MAA} \approx 0.330245$.

The physical meaning of MAA can be illustrated by considering an fODF that has a constant nonzero value over a surface area fraction κ and is zero otherwise. We then simply have

$$\mathrm{MAA} = \sqrt{1 - \sqrt{\kappa}}\,. \tag{28}$$

Thus an fODF that is spread out over a large surface area has a low MAA while a sharply peaked fODF has a high MAA. Note that, for this example, the MAA is insensitive to the details of the shape of the surface area where the fODF is nonzero.

2.7 | Imaging

Three healthy volunteers were scanned with a 32 channel head coil on a 3 T Prisma$^{\mathrm{fit}}$ MRI scanner (Siemens Healthineers, Erlangen, Germany). The coil combine mode was set to adaptive combine for all diffusion sequences in order to minimize noise bias.[33] All subjects gave informed consent under a protocol approved by the institutional review board of the Medical University of South Carolina.

FBI data were acquired for three different b-value shells with b = 5000, 8000, and 10 000 s/mm^2 using a monopolar diffusion sequence and 256 uniformly distributed diffusion encoding directions on a half sphere. For each b-value shell, a total of 42 axial slices were obtained with a slice thickness of 3 mm, a field of view of 222 × 222 mm^2, and an acquisition matrix of 74 × 74, thereby yielding 3 × 3 × 3 mm^3 isotropic voxels. The parallel imaging and slice acceleration factors were both set to 2, and the bandwidth was set to 1536 Hz/pixel. For the b = 5000 s/mm^2 shell, the T_E was 83 ms, the repetition time (T_R) was 3500 ms, the diffusion time (Δ) was 40.1 ms, and the diffusion pulse duration (δ) was 22.1 ms; for the b = 8000 s/mm^2 shell, T_E was 99 ms, T_R was 3900 ms, Δ was 48.7 ms, and δ was 30.1 ms; for the b = 10 000 s/mm^2 shell, T_E was 108 ms, T_R was 4000 ms, Δ was 53.2 ms, and δ was 34.6 ms. For each b-value, a set of 10 b = 0 volumes was collected with matched imaging parameters, and one b = 0 volume was collected with the phase encoding direction reversed to facilitate corrections for susceptibility distortion. The entire acquisition for the b = 8000 s/mm^2 shell was repeated within the same scan session to allow for assessment of reproducibility.

In order to identify white matter voxels, diffusional kurtosis imaging[34,35] data were also acquired with the same monopolar diffusion sequence. The imaging parameters were identical to those for the FBI scan with b = 8000 s/mm^2 except that b-values of 1000 and 2000 s/mm^2 were used along with 30 diffusion encoding directions for each of these two b-value shells.

To determine voxelwise estimates of the intra-axonal diffusivity D_a, a previously described custom triple diffusion encoding (TDE) MRI pulse sequence was employed.[36] The imaging parameters were matched to the b = 8000 s/mm^2 FBI scan except that T_E was 122 ms, Δ was 37.1, δ was 18.6 ms, the axial b-value was 4000 s/mm^2, and the number of diffusion encoding directions was 64. TDE data were obtained with the radial gradients both switched on (radial b-value = 307 s/mm^2) and switched off. As for the other diffusion scans, 10 matched b = 0 volumes were collected along with a single reversed phase encoding b = 0 volume.

2.8 | Data processing

Preprocessing of the dMRI data utilized a Python implementation (https://github.com/m-ama/PyDesigner) of the DESIGNER pipeline.[37] This included denoising with Rician bias correction,[38] Gibbs ringing correction,[39] susceptibility distortion correction,[40] co-registration,[41] eddy current correction,[41] and Gaussian smoothing with a full width at half maximum of 1.25 to further suppress the effects of noise and Gibbs ringing. This pipeline also calculated parametric maps of standard diffusion measures including the fractional anisotropy (FA) and mean kurtosis (MK).

Voxelwise maps for the intrinsic intra-axonal diffusivity, D_a, were obtained from the TDE data using a previously described method.[36,42] Specifically, we used the formula

$$D_a = \frac{1}{b_\perp} \ln\left(\frac{\bar{S}_1}{\bar{S}_2}\sqrt{\frac{b_\parallel}{b_\parallel - b_\perp}}\right), \quad (29)$$

where $b_{\parallel}$ is the axial b-value, $b\perp$ is the radial b-value, $\bar{S}_1$ is the direction-averaged TDE signal with the radial gradient switched off, and $\bar{S}_2$ is the direction-averaged TDE signal with the radial gradient switched on. The average D_a values across all white matter voxels were found to be 2.14 ± 0.14 $\mu m^2/ms$, 2.10 ± 0.21 $\mu m^2/ms$, and 2.13 ± 0.17 $\mu m^2/ms$, for Subjects 1, 2, and 3, respectively. White matter was defined as all voxels in the cerebrum with MK ≥ 1.[43]

The FBI data for each b-value shell were expanded in spherical harmonics using the method of least squares, and fODFs were determined for all white matter voxels by applying Equations 5 and 10 with L set to either 4, 5, or 6 and with D_0 set to either D_a, 3 $\mu m^2/ms$, or ∞. Because some fODFs calculated in this way take on unphysical negative values in some directions (due, for example, to Gibbs phenomena related to the truncation of the spherical harmonic expansion), all fODFs were rectified according to an optimized method.[44] This method makes the fODFs nonnegative in way that minimizes the mean square difference between the original fODF, obtained from Equations 5 and 10, and the final rectified fODF. For this study, rectification was essential in order to calculate Matusita distances and anisotropies, since these necessitate taking the square root of the fODFs. However, the effect of rectification on most fODFs was minor.[44] HEAP maps for fODFs in their local frames of reference were generated by applying Equations 19–23.

The MAA value for an fODF was calculated from Equation 26, while the FAA was obtained from[6]

$$\mathrm{FAA} = \sqrt{\frac{3\sum_{m=-2}^{2}\left|c_2^m\right|^2}{5\left|c_2^0\right|^2 + 2\sum_{m=-2}^{2}\left|c_2^m\right|^2}}. \tag{30}$$

To find the Matusita distance, D_M, between two fODFs, we used Equation 25 with the integral being evaluated numerically.

3 | RESULTS

The effect on fODF representations of rotating from the original laboratory frame of reference (global frame) to a local frame of reference based on the eigenvectors of the tensor A is illustrated in Figure 3. The leftmost column shows the HEAP maps in the global frame for fODFs from four different white matter voxels all taken from a single subject. The central column shows the same fODFs in the local frames. After the change in coordinates, the main weights of the fODFs are concentrated near the centers of the maps. The rightmost column shows the corresponding three-dimensional glyphs. The fODFs for the HEAP maps in this figure and those below were rescaled to have a maximum value of unity for the sake of visual clarity. However, for all quantitative calculations, the normalization of Equation 2 was employed.

A comparison of fODFs from two different scans is shown in Figure 4 for the same four voxels as in Figure 3. For $2L = 8$, a high degree of reproducibility is apparent and quantified by low Matusita distances between the two scans of 0.07 to 0.13. With an increased

maximum degree of spherical harmonic expansion the angular resolution improves, but the reproducibility is diminished, as reflected in the higher Matusita distances. For $2L = 10$ the reproducibility is still good, with Matusita distances ranging from 0.16 to 0.21, but for $2L = 12$ the Matusita distances vary from 0.36 to 0.45 in Voxel 4. This poorer reproducibility for $2L = 12$ reflects the effects of signal noise on the higher degree harmonics that may be amplified by aliasing due to insufficient data sampling. Even with limited reproducibility, the FAA and MAA changed by at most a few percent across scans for all three choices of $2L$.

Distributions of voxelwise Matusita distances between fODFs obtained for the first and second scans with $b = 8000$ s/mm^2 and $D_0 = D_a$ for three subjects are given in Figure 5. The distances become smaller with decreasing $2L$. This is because decreasing $2L$ has a smoothing effect on the fODFs that suppresses the effects of signal noise. However, this same change also reduces the angular resolution of the fODFs. Thus, the choice of $2L$ constitutes a compromise between precision and accuracy. The smoothing effect of decreasing $2L$ is illustrated in Figure 6 for a single voxel.

Also shown in Figure 6 is the smoothing effect of increasing D_0, which is most apparent for $2L = 12$. Supporting Figure S3 shows, for b = 8000 s/mm^2, the distribution of Matusita distances between fODFs with $D_0 = D_a$ and $D_0 = D_f$ and between fODFs with $D_0 = D_a$ and $D_0 = \infty$. The distances for the first difference are smaller than for the second, reflecting a better accuracy for $D_0 = D_f$ in comparison with $D_0 = \infty$. The distances decrease when $2L$ is reduced, because of the aforementioned smoothing effect of lowering the maximum degree of the spherical harmonic expansion.

Figure 7 compares the fODFs for the same voxel as in Figure 6 for b-values of 5000, 8000, and 10 000 s/mm^2. Note that the smoothing effect of increasing D_0 is diminished for the larger b-values, as expected from the fact that the generalized Funk transform approaches the classical Funk transform in the limit that the control parameter S goes to infinity. Distribution of Matusita distances for the same three b-values for all white matter voxels from each of three subjects are given in Supporting Figure S4. As for Supporting Figure S3, the distances are between fODFs with $D_0 = D_a$ and $D_0 = D_f$ and between fODFs with $D_0 = D_a$ and $D_0 = \infty$. Note how the distribution plots shift to smaller values as the b-value is increased. Additional distribution plots are given in Supporting Figure S5, showing Matusita distances between fODFs with different b-values and with different values for $2L$.

Maps for the three anisotropies FA, FAA, and MAA for a single anatomical slice from each of three subjects appear in Figure 8. While there are strong qualitative similarities, there are also clear differences that reflect the distinct information that each type of anisotropy provides. The traditional FA quantifies the anisotropy of the diffusion tensor of the full tissue, but the FAA quantifies the tensor anisotropy of just water confined to the intra-axonal compartment. The MAA is also specific to the intra-axonal water pool, but differs from the FAA in being sensitive to spherical harmonic components of the fODF with degrees greater than 2.

Distribution plots for FA, FAA, and MAA for the three subjects are shown in Figure 9. The mean FA values are 0.43 ± 0.13, 0.43 ± 0.14, and 0.44 ± 0.14 for Subjects 1, 2, and 3, respectively; the mean FAA values are 0.54 ± 0.13, 0.54 ± 0.14, and 0.54 ± 0.14; the mean MAA values are 0.40 ± 0.07, 0.41 ± 0.07, and 0.41 ± 0.07. Pairwise correlation plots for the three anisotropies with data from three subjects are given in Figure 10. Note that FA and FAA are more strongly correlated with each other than either is with MAA. Nevertheless, the FAA and MAA are tightly correlated for FAA values above 0.8, which represent voxels with narrow distributions of axon directions.

An advantage of employing the local frame of reference for each fODF is that this facilitates comparison of fODFs across voxels. An example is provided in Figure 11, which shows average fODFs over all white matter voxels for $2L = 8,10,12$ from each of three subjects. Across all three subjects, the full widths at half maximum for these averages in the horizontal direction are 47.8° ± 2.9° with $2L = 8$, 43.5 ± 2.9 with $2L = 10$, and 39.2 ± 4.0 with $2L = 12$, where we have indicated the intersubject standard deviations. These values are all larger than the angular resolutions listed in Table 1, reflecting dispersion of the intra-voxel axonal orientations. That the widths decrease with increasing $2L$ suggests that a significant fraction of fODFs have true widths smaller than the angular resolution for $2L = 10$ (ie 22°). As a second example, Figure 12 shows, for selected anatomical slices, maps of the Matusita distances between the fODFs from each voxel and the average fODF across the whole white matter. Large distances indicate white matter regions having atypical fODFs.

4 | DISCUSSION

The observation of large diffusion anisotropy in white matter was a watershed event in the history of dMRI.[45,46] It has sparked several major developments in the field, such as diffusion tensor imaging[47] and fiber tractography,[48–50] and continues to be a topic of intensive study. With improving methods for analyzing and interpreting dMRI data, as well as better scanner technology, the ability to quantify diffusion anisotropy has steadily progressed. An important step was the introduction of fODF approaches which focus on the main source of diffusion anisotropy, namely water confined inside axons. These have proven valuable for both fiber tractography[4] and microstructural modeling.[5–8] Advancements in the measurement of fODFs now make it feasible to extract detailed information about fODF structure that go beyond identifying a few primary fiber bundle directions and supporting the calculation of compartmental diffusion parameters. However, systematic methods for exploiting this information are not currently well developed, which limits the application of fODF structure to the investigation and assessment of white matter disease.

This study has considered several issues that are relevant for the measurement and utilization of high fidelity fODFs, defined as representations with adequate resolution to capture the main angular variation of axonal fiber bundles and with minimal errors due to sampling and noise. First, we have discussed the relationship between the angular resolution of an fODF map, which is vital to properly interpret its physical meaning, and the number of terms included in its representation as a spherical harmonic expansion. We find that the achievable angular resolution improves approximately as the total number of terms raised to the negative one-half power, as expressed by Equation 13. Second, we have argued that

the number of diffusion encoding directions should be about 2–3 or more multiplied by the number of expansion terms, if substantial sampling errors are to be avoided. Third, we have noted, for FBI, that the noise variance of the higher spherical harmonic expansion coefficients decreases with increasing b-value up to a limit that grows quadratically with the harmonic degree for finite D_0 (Equation 17). This favors larger b-values if one wishes to accurately depict fODF fine structure. Larger b-values are also beneficial in that they more fully suppress the confounding effect of signal from the extra-axonal compartment, as well as reducing the dependence of the fODF on the choice of the diffusivity scale D_0. In practice, b-values in the range of 6000 to 12 000 s/mm^2 are often appropriate for obtaining high fidelity fODFs when applying FBI to human data acquired on state-of-the-art clinical 3 T scanners. The achievable interscan reproducibility of fODFs obtained with angular resolutions of 27° to 19° is illustrated in Figures 4 and 5 for a b-value of 8000 s/mm^2. Fourth, in plotting fODFs, we have proposed using, as shown in Figure 3, local reference frames that are tied to each fODF's individual structure rather than to a global reference frame. This allows fODF structure to be compared independently of spatial orientation. Finally, we have suggested that the Matusita distance and the associated MAA can be useful in quantifying subtle changes across subjects in fODF structure, which may be related to aging and disease.

While these issues have here all been discussed in the context of FBI, several of our conclusions apply also to other methods of fODF estimation. For example, some of our results for the angular resolution of fODF maps are also relevant to the constrained spherical deconvolution approach,[51] and our proposals to use local reference frames and the Matusita distance are generally applicable. However, our analysis of the effects of signal noise is specific to FBI, since this depends on the details of the fODF calculation. Also, specific to FBI are considerations of the diffusivity scale D_0. The standard choices for this parameter are D_a, $D_f \approx 3.0$ μm^2/ms, or ∞. For high fidelity fODFs, $D_0 = D_a$ is preferred, but $D_0 = D_f$ is also quite acceptable. On the other hand, setting $D_0 = \infty$ may cause significant fODF blurring, as illustrated in Figures 6 and 7.

An important observation of this study is that high fidelity fODFs obtained with even a modest amount of oversampling require the use of a relatively large number of diffusion encoding directions. For example, with an oversampling factor of 3, Table 1 implies that 84 directions are sufficient for an angular resolution of about 34°, 135 directions are sufficient for a resolution of about 27°, 198 directions are sufficient for a resolution of about 22°, and 273 directions are sufficient for a resolution of about 19°. Since the angular spread of axonal fiber bundles can be as low as 18°,[23] fewer than 84 diffusion encoding directions is likely inadequate to achieve a high fidelity representation of the fODF throughout white matter.

The angular resolution determines the ability to resolve distinct peaks of a given fODF, which typically requires a resolution that is smaller than the angle of separation and is relevant to fiber tractography in white matter regions with intersecting fiber bundles. The angular resolution also sets the minimum amount of axonal dispersion (ie fanning) that can be quantified and is important for delineation of peak shape. It should be emphasized, however, that the accuracy of the fODF peak directions may be substantially better than the angular resolution, allowing white matter fiber tractography to be successfully performed

with fewer directions than are needed for high fidelity fODFs. In particular, the estimated peak direction for a single axially symmetric fiber bundle is independent of the fODF angular resolution, so a low resolution is adequate for fiber tractography in such cases.

An advantage of high fidelity fODFs is that they support a more refined notion of axon orientation anisotropy. Conventionally, diffusion anisotropy is quantified with the FA, but this reflects anisotropy of both the intra-axonal and extra-axonal spaces. The FAA is specific to axons, but it is only sensitive to spherical harmonics up to degrees of $2L = 2$ and therefore does not reflect the fine details of fODFs captured in the higher harmonics. For this reason, we have introduced the MAA, which is both specific to axons and sensitive to harmonics of all degrees. Although we have found a strong correlation between the FAA and MAA of about r = 0.83 for healthy white matter (Figure 10), the fraction of the variance in MAA that is unexplained by the FAA is still over 30%. Equation 27 gives a specific example of a simple fODF where the FAA and MAA are markedly different.

A summary of the effects of adjusting the main parameters that impact fODF quality along with specific recommendations is given in Table 2. The recommendations are appropriate for 3 T clinical MRI in healthy adult subjects. There is currently little information on the validity and application of FBI for young children and for adults with severe brain pathology, and caution is advised when using FBI with these groups. The feasibility of the recommended parameter choices may depend on the available scanner hardware and software.

Most of the prior literature on fODFs has focused on obtaining the peak directions with little consideration of fODF fine structure. This is partly because of the strong interest in fiber tractography, but may also reflect an appreciation that typical dMRI scans have too few diffusion encoding directions and too low b-values to support the calculation of high fidelity fODFs. However, recent improvements in scanner hardware, scanner software, and data preprocessing techniques have made it much more practical to increase the number of directions and b-value to an extent sufficient to achieve high fidelity. In particular, MRI systems with maximum magnetic field gradient amplitudes of 80 mT/m allow high b-value data to be obtained in white matter with good SNR,[9] pulse sequences with simultaneous multislice capability can accelerate data acquisition by factors of 2 to 4,[52] and advanced denoising techniques can substantially improve data quality.[38] These innovations provide exciting opportunities for exploring how the fine structure of fODFs is altered by disease and aging. In order to support future work in this direction, we have discussed, in this paper, general conceptual issues relevant to constructing and applying high fidelity fODF representations and provided several examples obtained with FBI.

5 | CONCLUSION

We have demonstrated how to construct high fidelity fODFs in white matter with FBI. In particular, conditions have been derived for guiding the choices of the number of diffusion encoding directions and the b-value. The number of directions should be sufficient to mitigate sampling errors, while increasing the diffusion weighting can be beneficial for improving fODF accuracy as long as adequate SNR can be maintained. In order to facilitate

the comparison of fODFs across voxels, a local frame of reference has been introduced so that differences in fODF structure can be assessed independently of spatial orientation. The MAA is proposed as a means of quantifying angular variability of individual fODFs that is more sensitive to the finer structural details than established indices of anisotropy.

Supplementary Material

Refer to Web version on PubMed Central for supplementary material.

ACKNOWLEDGEMENTS

This work was supported, in part, by National Institutes for Health research grants F31NS108623 (to H. Moss) and R01AG054159. We are grate-ful to an anonymous reviewer who contributed a key insight that substantially improved our discussion of angular resolution.

Funding information National Institutes of Health; Health research, Grant/Award Numbers: F31NS108623, R01AG054159

APPENDIX

APPENDIX

APPENDIX A: DEFINITION OF FODF

To give a mathematical definition of the fODF for a given voxel, we first introduce a function h(r) that is unity for all positions r inside the voxel and vanishes for all positions outside the voxel. We also assume that the geometry of the ith axon's track is well described by a principal curve $\mathbf{R}^{(i)}(\boldsymbol{\tau})$ that is parametrized by its arc length $\boldsymbol{\tau}$. While there are several methods of constructing principal curves,[53,54] one expects these to yield similar paths for thin, tubular objects such as axons. The tangent vector for the ith axon at $\boldsymbol{\tau}$ is then

$$\mathbf{T}^{(i)}(\tau) = \frac{d}{d\tau}\mathbf{R}^{(i)}(\tau)\,. \tag{A1}$$

By construction, $\left|\mathrm{T}^{(i)}(\tau)\right| = 1$. Let us also define $V^{(i)}(\tau, \tau_{\mathrm{O}})$ as the volume of the ith axon contained between the point $\boldsymbol{\tau}$ and some initial point $\boldsymbol{\tau}_0$.Here the axonal volume only refers to space contained inside the axolemma and excludes the surrounding myelin sheath.

In terms of the axon principal curves, the fODF may be expressed as

$$F(\mathbf{u}) = \frac{1}{2\pi V_{\mathrm{a}}}\sum_i \int d\tau \left|\frac{d\mathbf{V}^{(i)}(\tau,\tau_0)}{d\tau}\right| h\left[\mathbf{R}^{(i)}(\tau)\right] \left\{\delta\left[\mathbf{u}\cdot\mathbf{T}^{(i)}(\tau) - 1\right] + \delta\left[\mathbf{u}\cdot\mathbf{T}^{(i)}(\tau) + 1\right]\right\}, \tag{A2}$$

where δ(x) is the Dirac delta function,

$$V_{\mathrm{a}} \equiv \sum_i \int d\tau \left|\frac{dV^{(i)}(\tau,\tau_0)}{d\tau}\right| h\left[\mathbf{R}^{(i)}(\tau)\right] \tag{A3}$$

is the total axonal volume within the voxel, and with the summations in Equations A2 and A3 being taken over all axons that intersect the voxel. The argument u of the fODF is restricted to be a unit vector so that |**u**| = 1. One may confirm that Equation A2 is consistent with the normalization of Equation 2 and with the antipodal symmetry $F(-\mathrm{u}) = F(\mathrm{u})$. Including the axonal volume derivatives in Equations A2 and A3 is necessary for the contribution of each axon to the fODF to be proportional to its volume fraction. The initial point $\boldsymbol{\tau}_0$ is arbitrary and does not affect $F(\mathrm{u})$ since a change in $\boldsymbol{\tau}_0$ just shifts $V^{(i)}(\tau, \tau_0)$ by a constant that is independent of $\boldsymbol{\tau}$. The right-hand side of Equation A2 can be interpreted as the volume-weighted density of local tangents to the fibers' principal curves.

Since Equation A2 involves only morphological properties of axons, the fODF constitutes a physical property of neuronal cytoarchitecture. It could, in principle, be calculated from three-dimensional white matter histology,[55] although care should be taken that the fixation process does not excessively alter the axon shape.[56] As previously mentioned, there is still an unresolved question as to whether the fODF, as estimated with FBI, reflects only myelinated axons or both myelinated and unmyelinated axons.

A special case of interest is when all the axons are perfectly straight within the voxel. Then the tangent vectors are independent of $\boldsymbol{\tau}$, and Equation A2 simplifies to

$$F(\mathbf{u}) = \frac{1}{2\pi V_a} \sum_i V_a^{(i)} \left\{ \delta\left[u \cdot \mathbf{T}^{(i)} - 1\right] + \delta\left[\mathbf{u} \cdot \mathbf{T}^{(i)} + 1\right] \right\}, \tag{A4}$$

where $V_a^{(i)}$ is the volume for the ith axon within the voxel. Equation A4 simply gives the volume-weighted angular density of axon orientations. Although Equation A2 corresponds to a conventional notion of an fODF in the context of dMRI, alternative definitions are possible. For example, by including information related to the axon curvature, "asymmetric fiber orientation distributions" may be defined.[57] The results of this paper are not relevant in such cases and apply only to fODFs consistent with Equation A2.

APPENDIX B: GENERALIZED FUNK TRANSFORM

The classical Funk transform is a linear map of a function f defined on the surface of a unit sphere to another function $T_{\mathrm{F}}\{\mathrm{f}\}$ also defined on a unit sphere.[58–60] It is given explicitly by

$$T_{\mathrm{F}}\left\{f\right\}(\mathbf{u}) \equiv \int d\Omega_{\mathrm{n}} f(\mathbf{n}) \delta(\mathbf{u} \cdot \mathbf{n}), \tag{B1}$$

where **u** and **n** are unit vectors, δ(x) is the Dirac delta function, and the integral is taken over the entire surface of the unit sphere. Because of the delta function, the surface integral in Equation B1 reduces to a line integral for each direction **u** around a corresponding great circle of points orthogonal to u. The Funk transform was first applied to dMRI in the context of q-ball imaging.[61] It is sometimes referred to as the Funk-Radon transform because of its close connection to the Radon transform, which plays a central role in computed tomography.[62]

For FBI, one defines a generalized Funk transform as

$$\tilde{T}_F\left\{f\right\}(\mathbf{u}, s) \equiv \sqrt{\frac{s}{\pi}} \int d\Omega_n f(\mathbf{n}) \mathrm{e}^{-s(\mathbf{u}\cdot\mathbf{n})^2}, \tag{B2}$$

where S is an added control parameter that can be set to any positive value. One may show that

$$\lim_{s\to\infty} \tilde{T}_F\left\{f\right\}(\mathbf{u}, s) = T_F\left\{f\right\}(\mathbf{u}), \tag{B3}$$

so the generalized Funk transform reduces to the classical Funk transform for large s.[10] Roughly speaking, the generalized Funk transform can be thought of as a classical Funk transform where the line integral around the great circle has been replaced by an integral over a band with a width scaling as $1/\sqrt{s}$.

A crucial property of the generalized Funk transform is that the spherical harmonics are its eigenfunctions so that

$$\tilde{T}_F\{\mathrm{Y}_I^m\}(\mathrm{u}, s) = \tilde{\lambda}_1(s)\mathrm{Y}_I^m(\theta, \varphi), \tag{B4}$$

where (θ, φ) are the spherical angles for the direction vector u, $Y_I^m(\theta, \varphi)$ is the spherical harmonic of degree I and order m, and $\tilde{\lambda}_1(s)$ is the eigenvalue. For odd integer degrees, the eigenvalues vanish, so these spherical harmonics are in the null space of $\tilde{T}_F$. For even integer degrees, the eigenvalues are nonzero, allowing the inverse generalized Funk transform to be calculated as

$$\tilde{\mathbf{T}}_{\mathrm{F}}^{-1}\left(\mathrm{Y}_{2l}^m, \mathrm{u}\right) = \frac{1}{\tilde{\lambda}_{2I}(s)}\mathrm{Y}_{2l}^m(\theta, \varphi)\,. \tag{B5}$$

The even degree eigenvalues have the explicit formula

$$\tilde{\lambda}_{2l}(s) = 2\pi P_{2l}(0) g_{2l}(s), \tag{B6}$$

where $\mathrm{P_l(x)}$ is the Legendre polynomial of degree l, and

$$g_l(s) = s^{(l+1)/2} \frac{\Gamma\left(\frac{1}{2}+1\right)}{\Gamma\left(I+\frac{3}{2}\right)^1} F_1\left(\frac{1}{2}+\frac{1}{2}; I+\frac{3}{2}; -s\right) \tag{B7}$$

with $\Gamma(x)$ being the gamma function and ${}_1F_1(a; c; x)$ being the confluent hypergeometric function of the first kind.[10] As S approaches infinity, the function $\mathrm{g_l(s)}$ approaches unity. Thus we have the limit

$$\lim_{s\to\infty} \tilde{\lambda}_{2l}(s) = 2\pi P_{2l}(0)\,. \tag{B8}$$

A useful approximation is[10]

$$g_1(s) \approx \exp\left[-\frac{I(I+1)}{4s}\right]. \tag{B9}$$

We also have the special case

$$g_0(s) = \mathrm{erf}(\sqrt{s}). \tag{B10}$$

Plots of $\tilde{\lambda}_{2I}(s)$ for several values of I are given by Figure S1 of the Supporting Information.

Abbreviations:

dMRI	diffusion MRI
FA	fractional anisotropy
FAA	fractional anisotropy axonal
FBI	fiber ball imaging
fODF	fiber orientation density function
HEAP	hemispheric equidistant azimuthal projection
MAA	Matusita anisotropy axonal
MK	mean kurtosis
PSF	point spread function
SNR	signal-to-noise ratio
TDE	triple diffusion encoding
$\mathbf{T_E}$	echo time
$\mathbf{T_R}$	repetition time

REFERENCES

1. Tournier JD, Calamante F, Gadian DG, Connelly A. Direct estimation of the fiber orientation density function from diffusion-weighted MRI data using spherical deconvolution. NeuroImage. 2004;23(3):1176–1185. [PubMed: 15528117]
2. Alexander DC. Multiple-fiber reconstruction algorithms for diffusion *MRI*. Ann N Y Acad Sci. 2005;1064(1):113–133. [PubMed: 16394152]
3. Tournier JD. Diffusion MRI in the brain—theory and concepts. Prog Nucl Magn Reson Spectrosc. 2019;112:1–16. [PubMed: 31481155]
4. Jeurissen B, Descoteaux M, Mori S, Leemans A. Diffusion MRI fiber tractography of the brain. NMR Biomed. 2019;32(4):e3785. [PubMed: 28945294]
5. Raffelt DA, Tournier JD, Smith RE, et al. Investigating white matter fibre density and morphology using fixel-based analysis. NeuroImage. 2017;144(Pt A):58–73. [PubMed: 27639350]

6. McKinnon ET, Helpern JA, Jensen JH. Modeling white matter microstructure with fiber ball imaging. NeuroImage. 2018;176:11–21. [PubMed: 29660512]
7. Lyon M, Welton T, Varda A, et al. Gender-specific structural abnormalities in major depressive disorder revealed by fixel-based analysis. NeuroImage Clin. 2019;21:101668.
8. Bryant L, McKinnon ET, Taylor JA, et al. Fiber ball white matter modeling in focal epilepsy. Hum Brain Mapp. 2021;42(8):2490–2507. [PubMed: 33605514]
9. Moss HG, McKinnon ET, Glenn GR, Helpern JA, Jensen JH. Optimization of data acquisition and analysis for fiber ball imaging. NeuroImage. 2019;200:690–703. [PubMed: 31284026]
10. Jensen JH, Glenn GR, Helpern JA. Fiber ball imaging. NeuroImage. 2016;124(Pt A):824–833. [PubMed: 26432187]
11. Grebenkov D. NMR survey of reflected Brownian motion. Rev Mod Phys. 2007;79(3):1077–1137.
12. McKinnon ET, Jensen JH, Glenn GR, Helpern JA. Dependence on *b*-value of the direction-averaged diffusion-weighted imaging signal in brain. Magn Reson Imaging. 2017;36:121–127. [PubMed: 27989904]
13. Novikov DS, Kiselev VG, Jespersen SN. On modeling. Magn Reson Med. 2018;79(6):3172–3193. [PubMed: 29493816]
14. Veraart J, Fieremans E, Novikov DS. On the scaling behavior of water diffusion in human brain white matter. NeuroImage. 2019;185:379–387. [PubMed: 30292815]
15. Holz M, Heil SR, Sacco A. Temperature-dependent self-diffusion coefficients of water and six selected molecular liquids for calibration in accurate ^{1}H NMR PFG measurements. Phys Chem Chem Phys. 2000;2(20):4740–4742.
16. Jelescu IO, Veraart J, Fieremans E, Novikov DS. Degeneracy in model parameter estimation for multi-compartmental diffusion in neuronal tissue. NMR Biomed. 2016;29(1):33–47. [PubMed: 26615981]
17. Dhital B, Reisert M, Kellner E, Kiselev VG. Intra-axonal diffusivity in brain white matter. NeuroImage. 2019;189:543–550. [PubMed: 30659959]
18. Sansò F. On the aliasing problem in the spherical harmonic analysis. J Geodesy. 1990;64:313–330.
19. Daducci A, McEwen JD, Van De Ville D, Thiran JP, Wiaux Y. Harmonic analysis of spherical sampling in diffusion *MRI*. Proc Int Soc Magn Reson Med.2011;19:5935.
20. Pusey E, Yoon C, Anselmo ML, Lufkin RB. Aliasing artifacts in MR imaging. Comput Med Imaging Graph. 1988;12(4):219–224. [PubMed: 3179974]
21. Heiland S. From A as in aliasing to Z as in zipper: artifacts in MRI. Clin Neuroradiol. 2008;18(1):25–36.
22. Costa M, Richter A, Koivunen V. Unified array manifold decomposition based on spherical harmonics and 2-D Fourier basis. IEEE Trans Signal Process.2010;58(9):4634–4645.
23. Ronen I, Budde M, Ercan E, Annese J, Techawiboonwong A, Webb A. Microstructural organization of axons in the human corpus callosum quantified by diffusion-weighted magnetic resonance spectroscopy of N-acetylaspartate and post-mortem histology. Brain Struct Funct. 2014;219(5):1773–1785. [PubMed: 23794120]
24. Pierpaoli C, Basser PJ. Toward a quantitative assessment of diffusion anisotropy. Magn Reson Med. 1996;36(6):893–906. [PubMed: 8946355]
25. Veraart J, Nunes D, Rudrapatna U, et al. Noninvasive quantification of axon radii using diffusion *MRI*. eLife. 2020;9:e49855.
26. Mohanty V, McKinnon ET, Helpern JA, Jensen JH. Comparison of cumulant expansion and q-space imaging estimates for diffusional kurtosis in brain.Magn Reson Imaging. 2018;48:80–88. [PubMed: 29306048]
27. Jespersen SN, Leigland LA, Cornea A, Kroenke CD. Determination of axonal and dendritic orientation distributions within the developing cerebral cortex by diffusion tensor imaging. IEEE Trans Med Imaging. 2011;31:16–32. [PubMed: 21768045]
28. Snyder JP, Voxland PM. An Album of Map Projections: U.S. Geological Survey Professional Paper 1453. US Government Printing Office, Washington, DC; 1989.
29. Gott JR III, Mugnolo C, Colley WN. Map projections minimizing distance errors. Cartographica. 2007;42(3):219–234.

30. Gott JR III, Goldberg DM, Vanderbei RJ. Flat maps that improve on the Winkel Tripel [preprint]. https://arxiv.org/abs/2102.08176. (accessed on April 16, 2021)
31. Cha SH. Comprehensive survey on distance/similarity measures between probability density functions. Int J Math Models Methods Appl Sci. 2007;1:300–307.
32. Matusita K. Decision rules, based on the distance, for problems of fit, two samples, and estimation. Ann Math Stat. 1955;26(4):631–640.
33. Dietrich O, Raya JG, Reeder SB, Ingrisch M, Reiser MF, Schoenberg SO. Influence of multichannel combination, parallel imaging and other reconstruction techniques on MRI noise characteristics. Magn Reson Imaging. 2008;26(6):754–762. [PubMed: 18440746]
34. Jensen JH, Helpern JA, Ramani A, Lu H, Kaczynski K. Diffusional kurtosis imaging: the quantification of non-Gaussian water diffusion by means of magnetic resonance imaging. Magn Reson Med. 2005;53(6):1432–1440. [PubMed: 15906300]
35. Jensen JH, Helpern JA. MRI quantification of non-Gaussian water diffusion by kurtosis analysis. NMR Biomed. 2010;23(7):698–710. [PubMed: 20632416]
36. Ramanna S, Moss HG, McKinnon ET, Yacoub E, Helpern JA, Jensen JH. Triple diffusion encoding MRI predicts intra-axonal and extra-axonal diffusion tensors in white matter. Magn Reson Med. 2020;83(6):2209–2220. [PubMed: 31763730]
37. Ades-Aron B, Veraart J, Kochunov P, et al. Evaluation of the accuracy and precision of the diffusion parameter EStImation with Gibbs and NoisE removal pipeline. NeuroImage. 2018;183:532–543. [PubMed: 30077743]
38. Veraart J, Novikov DS, Christiaens D, Ades-Aron B, Sijbers J, Fieremans E. Denoising of diffusion MRI using random matrix theory. NeuroImage. 2016; 142:394–406. [PubMed: 27523449]
39. Kellner E, Dhital B, Kiselev VG, Reisert M. Gibbs-ringing artifact removal based on local subvoxel-shifts. Magn Reson Med. 2016;76(5):1574–1581. [PubMed: 26745823]
40. Andersson JL, Skare S, Ashburner J. How to correct susceptibility distortions in spin-echo echo-planar images: application to diffusion tensor imaging.NeuroImage. 2003;20(2):870–888. [PubMed: 14568458]
41. Andersson JL, Sotiropoulos SN. An integrated approach to correction for off-resonance effects and subject movement in diffusion MR imaging. NeuroImage. 2016;125:1063–1078. [PubMed: 26481672]
42. Jensen JH, Helpern JA. Characterizing intra-axonal water diffusion with direction-averaged triple diffusion encoding MRI. NMR Biomed. 2018;31(7): e3930. [PubMed: 29727508]
43. Yang AW, Jensen JH, Hu CC, Tabesh A, Falangola MF, Helpern JA. Effect of cerebral spinal fluid suppression for diffusional kurtosis imaging. J Magn Reson Imaging. 2013;37(2):365–371. [PubMed: 23034866]
44. Moss HG, Jensen JH. Optimized rectification of fiber orientation density function. Magn Reson Med. 2021;85(1):444–455. [PubMed: 32710476]
45. Moseley ME, Cohen Y, Kucharczyk J, et al. Diffusion-weighted MR imaging of anisotropic water diffusion in cat central nervous system. Radiology.1990;176(2):439–445. [PubMed: 2367658]
46. Chenevert TL, Brunberg JA, Pipe JG. Anisotropic diffusion in human white matter: demonstration with MR techniques in vivo. Radiology. 1990;177(2):401–405. [PubMed: 2217776]
47. Basser PJ, Mattiello J, LeBihan D. MR diffusion tensor spectroscopy and imaging. Biophys J. 1994;66(1):259–267. [PubMed: 8130344]
48. Conturo TE, Lori NF, Cull TS, et al. Tracking neuronal fiber pathways in the living human brain. Proc Natl Acad Sci U *S* A. 1999;96(18):10422–10427. [PubMed: 10468624]
49. Mori S, Crain BJ, Chacko VP, Van Zijl PC. Three-dimensional tracking of axonal projections in the brain by magnetic resonance imaging. Ann Neurol.1999;45(2):265–269. [PubMed: 9989633]
50. Basser PJ, Pajevic S, Pierpaoli C, Duda J, Aldroubi A. In vivo fiber tractography using DT-MRI data. Magn Reson Med. 2000;44(4):625–632. [PubMed: 11025519]
51. Tournier JD, Calamante F, Connelly A. Robust determination of the fibre orientation distribution in diffusion MRI: non-negativity constrained superresolved spherical deconvolution. NeuroImage. 2007;35(4):1459–1472. [PubMed: 17379540]

52. Feinberg DA, Setsompop K. Ultra-fast MRI of the human brain with simultaneous multi-slice imaging. J Magn Reson. 2013;229:90–100. [PubMed: 23473893]
53. Kégl B, Krzyzak A, Linder T, Zeger K. Learning and design of principal curves. IEEE Trans Pattern Anal Machine Intell. 2000;22(3):281–297.
54. Bas E, Erdogmus D. Principal curves as skeletons of tubular objects: locally characterizing the structures of axons. Neuroinformatics. 2011;9(2–3):181–191. [PubMed: 21336847]
55. Leckenby JI, Chacon MA, Grobbelaar AO, Lichtman JW. Imaging peripheral nerve regeneration: a new technique for 3D visualization of axonal behavior. J Surg Res. 2019;242:207–213. [PubMed: 31085369]
56. Stradleigh TW, Greenberg KP, Partida GJ, Pham A, Ishida AT. Moniliform deformation of retinal ganglion cells by formaldehyde-based fixatives. J Comp Neurol. 2015;523(4):545–564. [PubMed: 25283775]
57. Reisert M, Kellner E, Kiselev VG. About the geometry of asymmetric fiber orientation distributions. IEEE Trans Med Imaging. 2012;31(6):1240–1249. [PubMed: 22345527]
58. Minkowski H. About bodies of constant width. Math Sb. 1904;25:505–508.
59. Funk P. Über Flächen mit lauter geschlossenen geodätischen Linien. Math Ann. 1913;74(2):278–300.
60. Funk P. Über eine geometrische Anwendung der Abelschen Integralgleichung. Math Ann. 1915;77(1):129–135.
61. Tuch DS. Q-ball imaging. Magn Reson *Med*. 2004;52(6):1358–1372. [PubMed: 15562495]
62. Zayed AI. A new perspective on the role of mathematics in medicine. J Adv Res. 2019;17:49–54. [PubMed: 31193335]

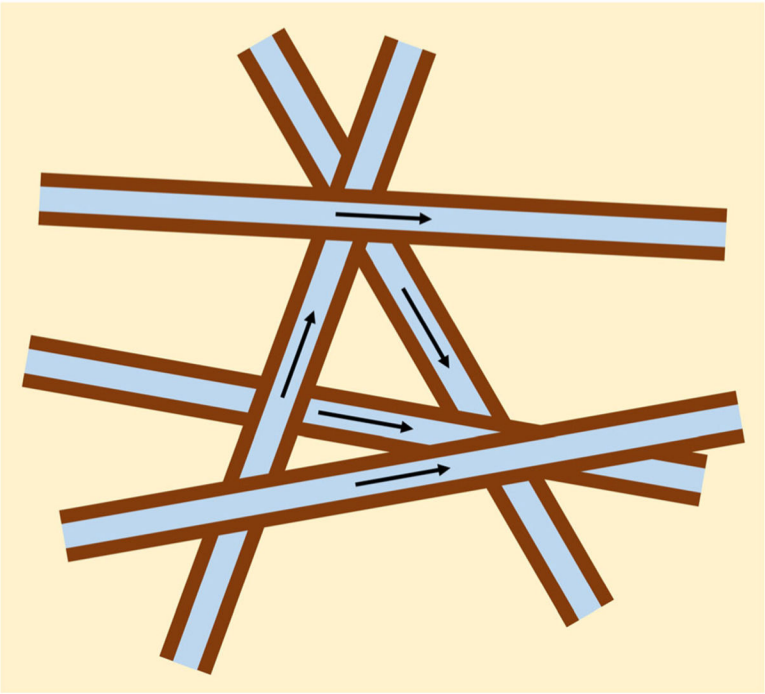

FIGURE 1.

The fODF gives the probability of an intra-axonal water molecule being located inside an axon oriented in a given direction. In the schematic diagram, the axoplasm is shown in blue, the myelin sheaths are shown in brown, and the extra-axonal space is shown in yellow. The directions of the axons are indicated by the arrows. By convention, the fODF is defined to have antipodal symmetry so that it is unchanged if the directions are rotated by 180°

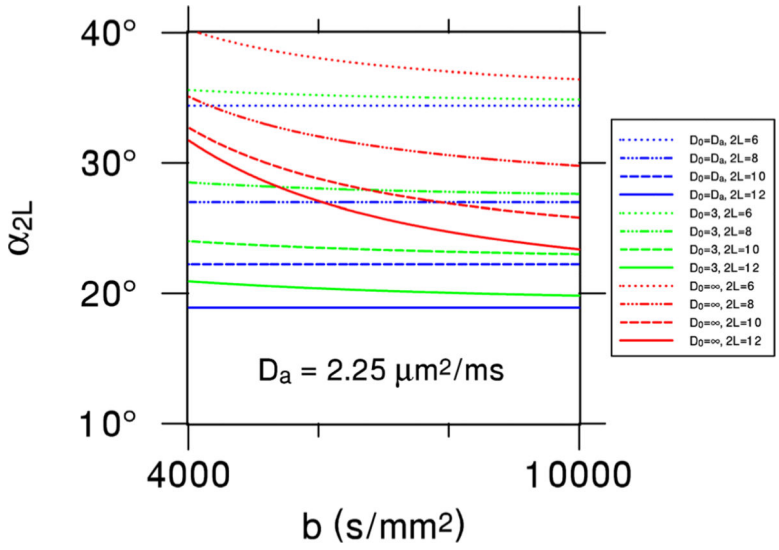

FIGURE 2.

The angular resolution α_{2L} as function of the *b*-value (b) for $D_0 = D_a$ (blue lines), $D_0 = 3\ \mu m^2/ms$ (green lines), $D_0 = \infty$ (red lines) with $2L = 6, 8, 10, 12$. For $D_0 = D_a$, α_{2L} is independent of b and decreases with increasing $2L$. For $D_0 > D_a$, α_{2L} decreases both with increasing b and with increasing $2L$. The angular resolutions for $D_0 = D_a$ and $D_0 = 3\ \mu m^2/ms$ are similar, but the resolution for $D_0 = \infty$ is substantially worse, especially for the lower *b*-values and higher $2L$-values. The plots for $D_0 = 3\ \mu m^2/ms$ and $D_0 = \infty$ are calculated using $D_a = 2.25\ \mu m^2/ms$; the plots for $D_0 = D_a$ are independent of the value of D_a and are consistent with Table 1

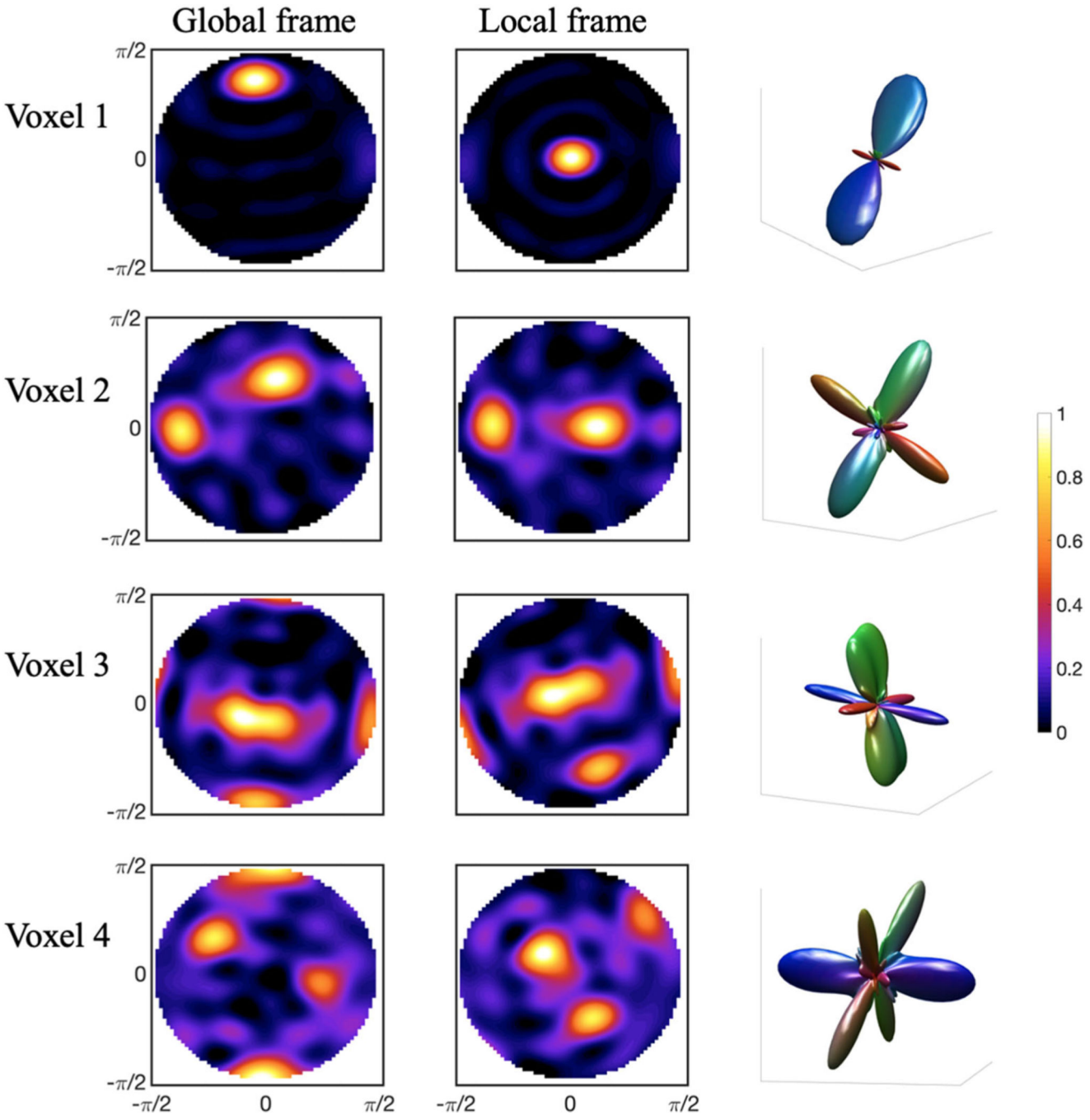

FIGURE 3.

The leftmost column shows HEAP maps for fODFs from four different white matter voxels from a single subject as they appear in a global reference frame defined by the laboratory coordinate system. The center column shows the same fODFs rotated to their individual local reference frames. In the local frames, the main weights of the fODFs are concentrated near the centers of the maps. The rightmost column shows the corresponding three-dimensional glyphs that are commonly used to depict fODFs. All fODFs are obtained from dMRI data with b = 8000 s/ mm^2 and are calculated with $2L = 10$ and $D_0 = D_a$. For

display purposes, the fODFs in the HEAP maps have all been individually rescaled to have a maximum value of unity. The distance from the center of each map reflects the polar angle θ while the azimuthal angle φ increases clockwise starting from 0 in the positive horizontal direction. The polar angle is restricted to the range 0 to $\pi/2$, and the azimuthal angle varies from 0 to 2π

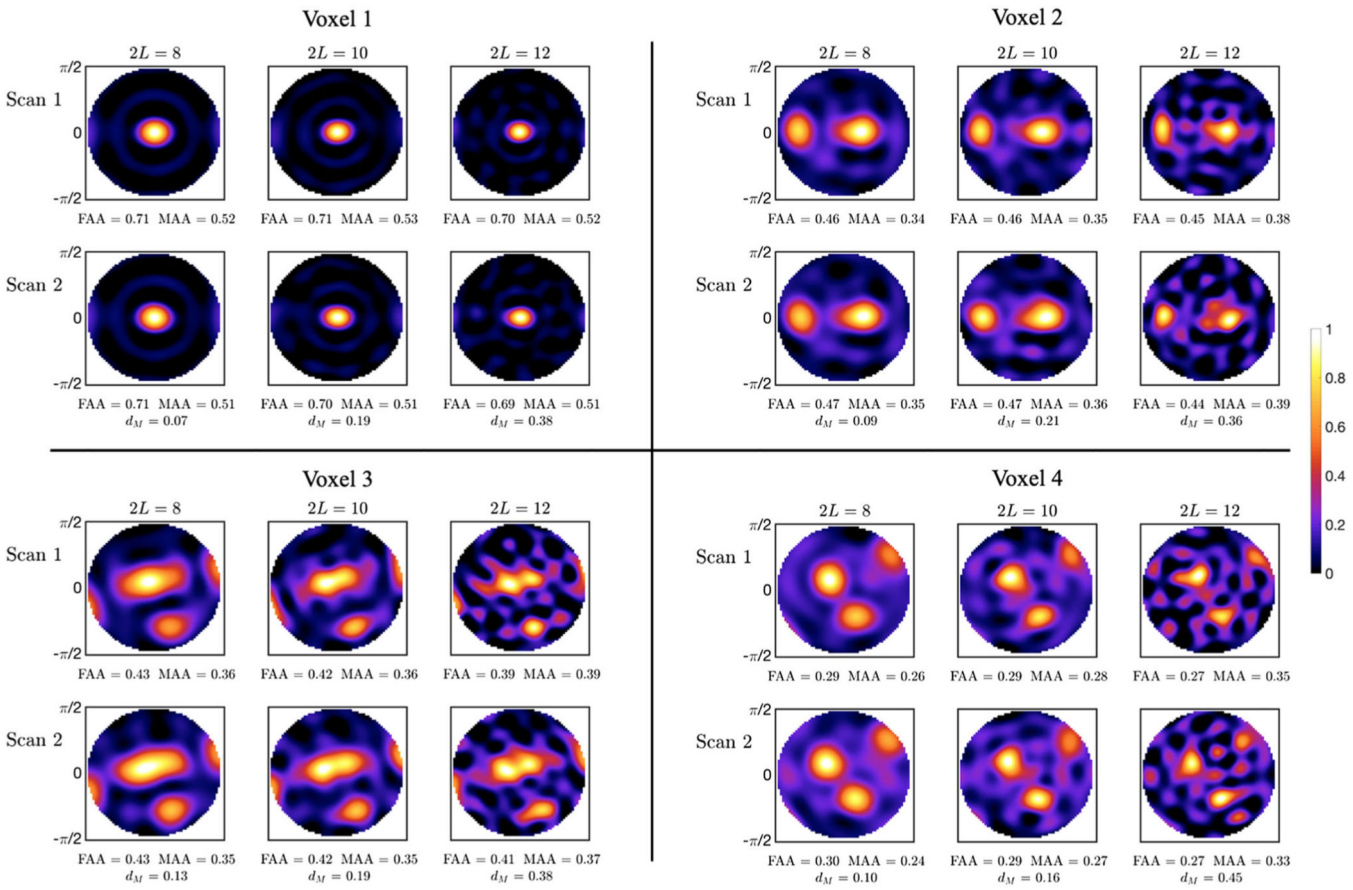

FIGURE 4.

Reproducibility of fODFs across two different scans for the same voxels as in Figure 3 with b = 8000 s/mm^2, $D_0 = D_a$, and $2L$ = 8,10,12. The FAA and MAA are indicated for each fODF along with the Matusita distance (D_M) between the first and second scans. The FAA and MAA are quite similar for both scans, but there is a non-negligible Matusita distance (D_M) that increases with $2L$. A lower $2L$ results in more reproducible fODFs but at the price of a worse angular resolution and sensitivity to fODF fine structure. Note that one can discern two peaks at the center of Voxel 3 for $2L$ = 12 that are merged into a single peak for $2L$ = 8. All maps are constructed using the fODFs' local frames of reference

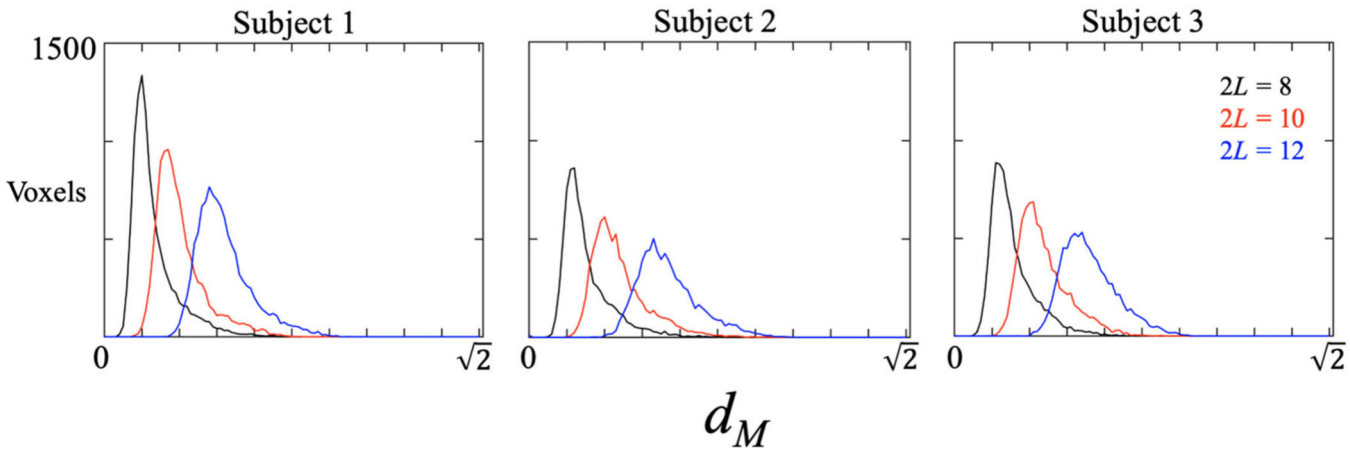

FIGURE 5.

Distribution plots of D_M values between the first and second FBI scans with b = 8000 s/mm^2 and $D_0 = D_a$ across all white matter voxels from three subjects. The D_M values increase with increasing $2L$ since the inclusion of higher harmonic degrees amplifies the sensitivity of the fODFs to signal noise. The plots are constructed using 100 bins over the full range of 0 to $\sqrt{2}$

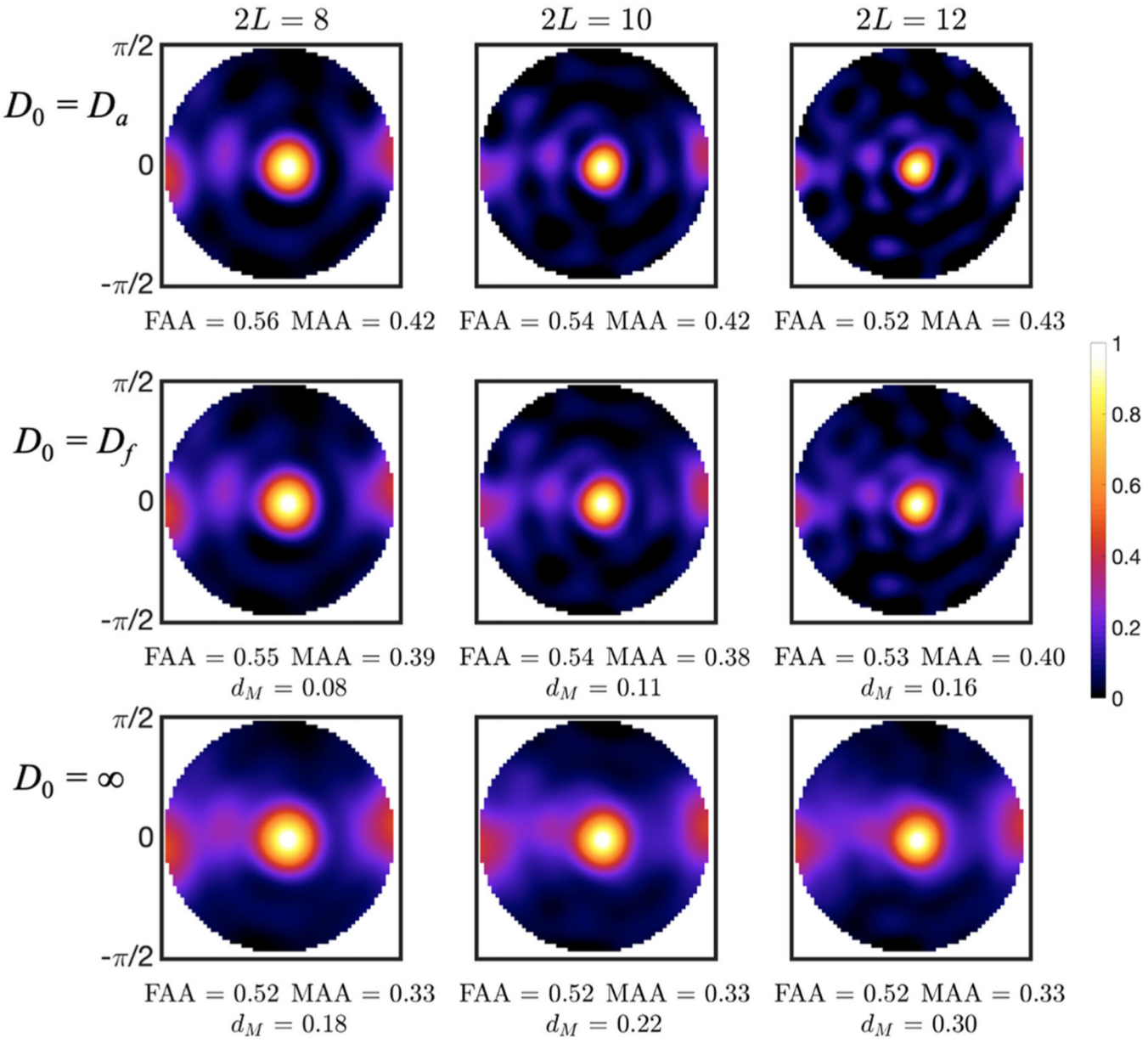

FIGURE 6.

Comparison of fODFs from a single voxel calculated with D_0 set to D_a, D_f (3 μm^2/ms), or ∞, for b = 8000 s/mm^2 and $2L$ = 8,10,12. The Matusita distances for $D_0 = D_f$ and $D_0 = \infty$ are relative to the fODFs with $D_0 = D_a$ and the same $2L$ values. The choice of $D_0 = D_f$ causes a slight blurring of the fODF in comparison to $D_0 = D_a$, which becomes more pronounced as $2L$ is increased and is reflected in D_M. The FAA and MAA values are only slightly affected. In contrast, use of $D_0 = \infty$ has more sizable effects that noticeably degrade fODF fidelity, particularly for $2L$ = 12. In general, setting $D_0 = D_a$ should give more accurate fODFs, but when D_a values are not available $D_0 = D_f$ provides a satisfactory alternative

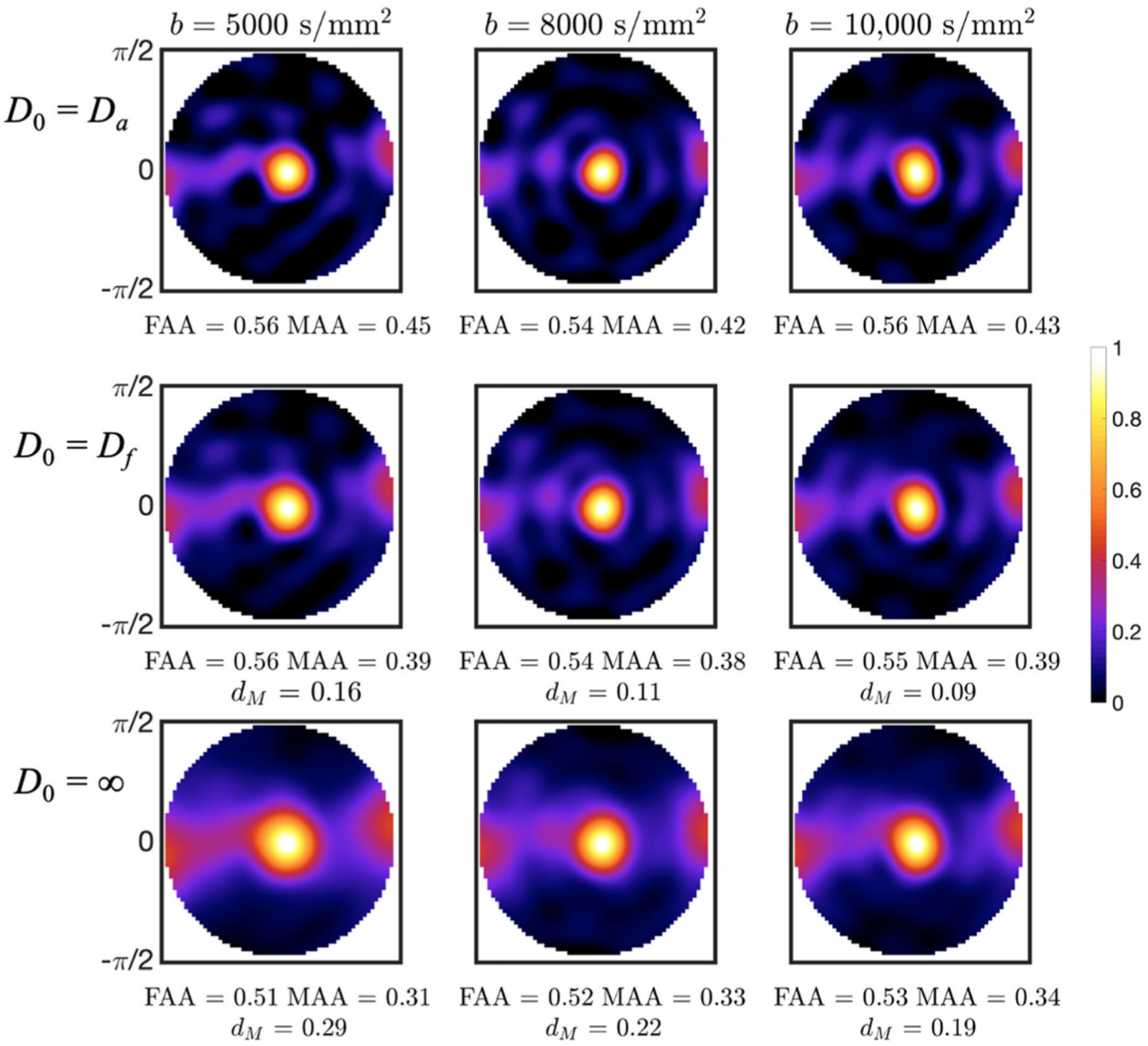

FIGURE 7.

Comparison of fODFs from a single voxel calculated with D_0 set to D_a, D_f, or ∞, for $2L$ = 10 and b = 5000, 8000, and 10 000 s/ mm^2. The Matusita distances for $D_0 = D_f$ and $D_0 = \infty$ are relative to the fODFs with $D_0 = D_a$ and the same b-values. The impact of the choice of D_0 diminishes with increasing b-value as reflected in the D_M values. The FAA and MAA values are only slightly changed as the b-value is increased, with the biggest effect being seen for $D_0 = \infty$

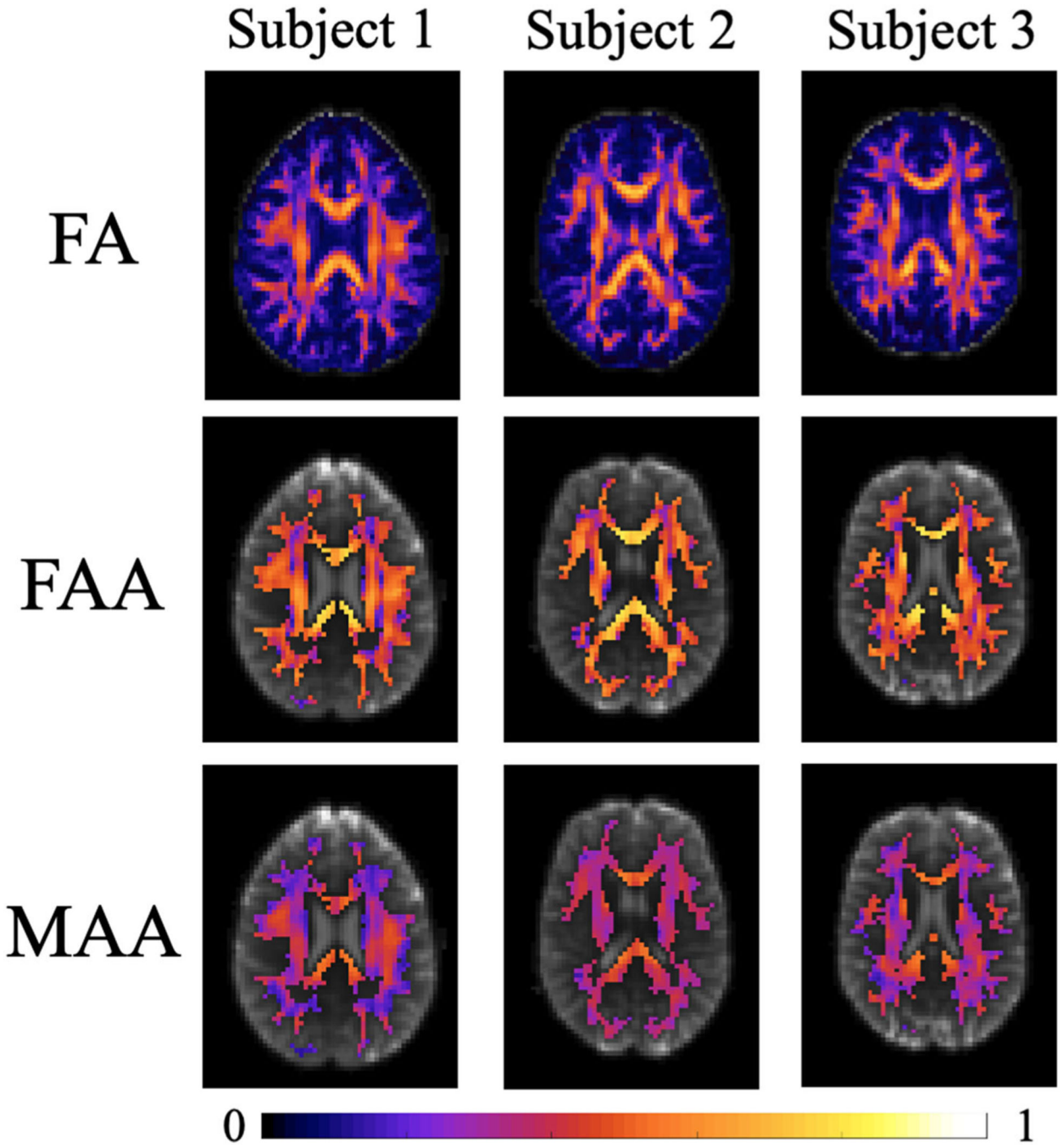

FIGURE 8.

FA, FAA, and MAA maps for a single anatomical slice from each of three subjects. The FA maps are derived from diffusional kurtosis imaging data. The FAA and MAA maps are calculated from fODFs using $2L = 10$ and $D_0 = D_a$ for dMRI data acquired with b = 8000 s/ mm^2. Since the FAA and MAA are only meaningful in white matter, only white matter voxels are shown in color for the maps of these two parameters. While all three anisotropies share qualitative features, they quantify different aspects of diffusion anisotropy. Both the

FAA and MAA are specific to the intra-axonal water pool, but the FA reflects the aggregate anisotropy of both intra-axonal and extra-axonal water

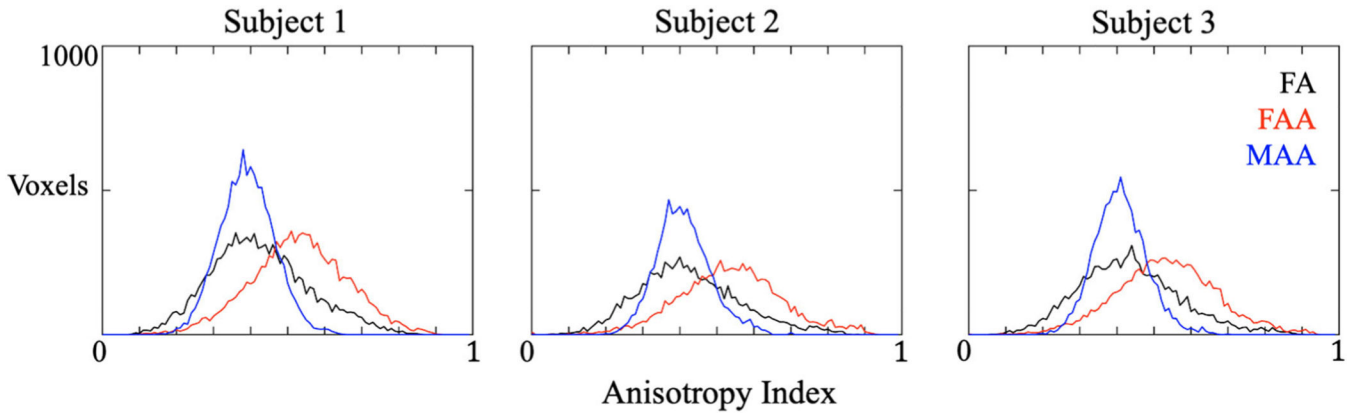

FIGURE 9.

Distribution of FA, FAA, and MAA across all white matter voxels for each of three subjects. Both FAA and MAA are determined using $2L = 10$ and $D_0 = D_a$ for data obtained with b = 8000 s/mm^2. The MAA distribution is more sharply peaked than either the FA or FAA. The plots are constructed using 100 bins over the full range of 0 to 1

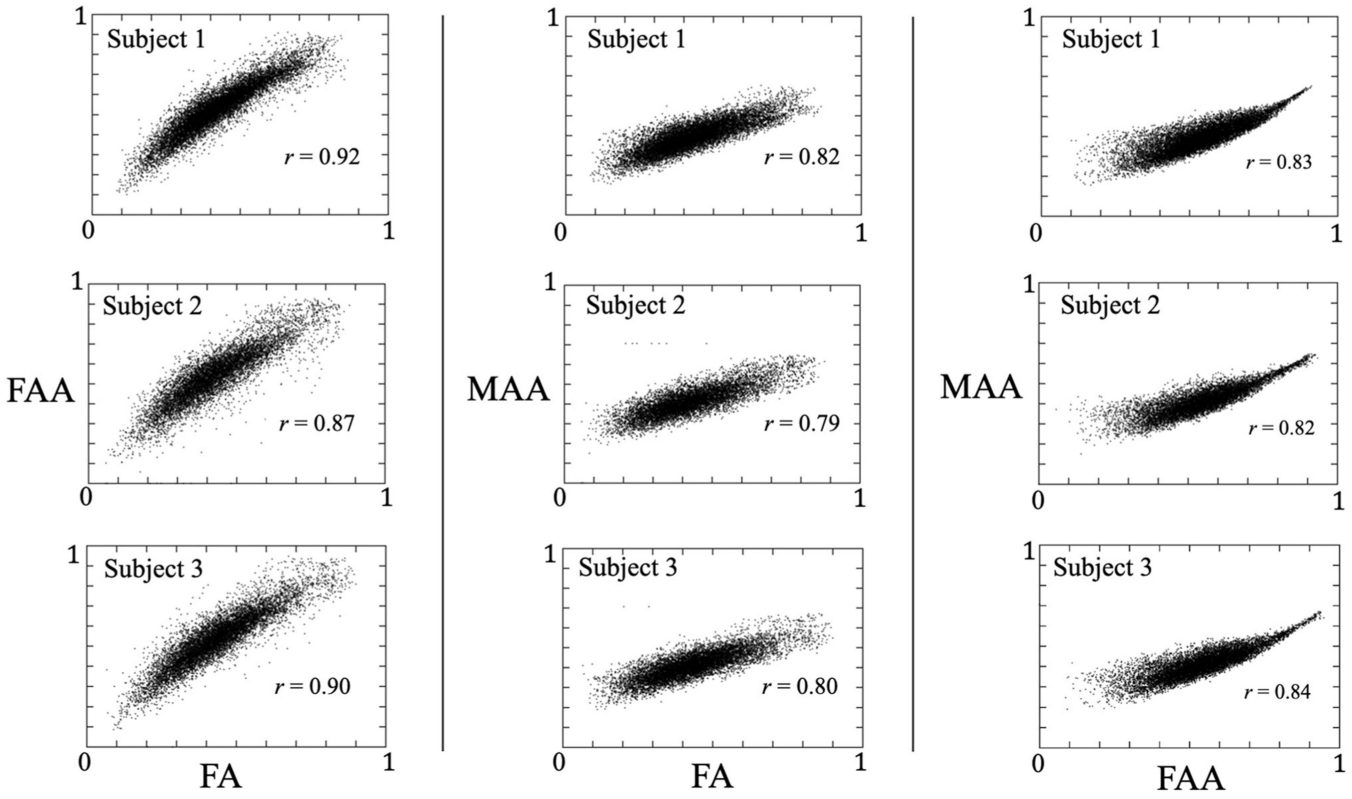

FIGURE 10.

Correlations between FA, FAA, and MAA across all white matter voxels from three subjects. All the correlation coefficients (r) are high, but MAA is less strongly correlated with either FA and FAA than is FAA with FA. However, in the rightmost column, MAA and FAA appear to be very highly correlated for FAA values above 0.8, which correspond to voxels where axons are mainly oriented in similar directions. Both FAA and MAA are for $2L = 10$, $D_0 = D_a$, and b = 8000 s/mm^2

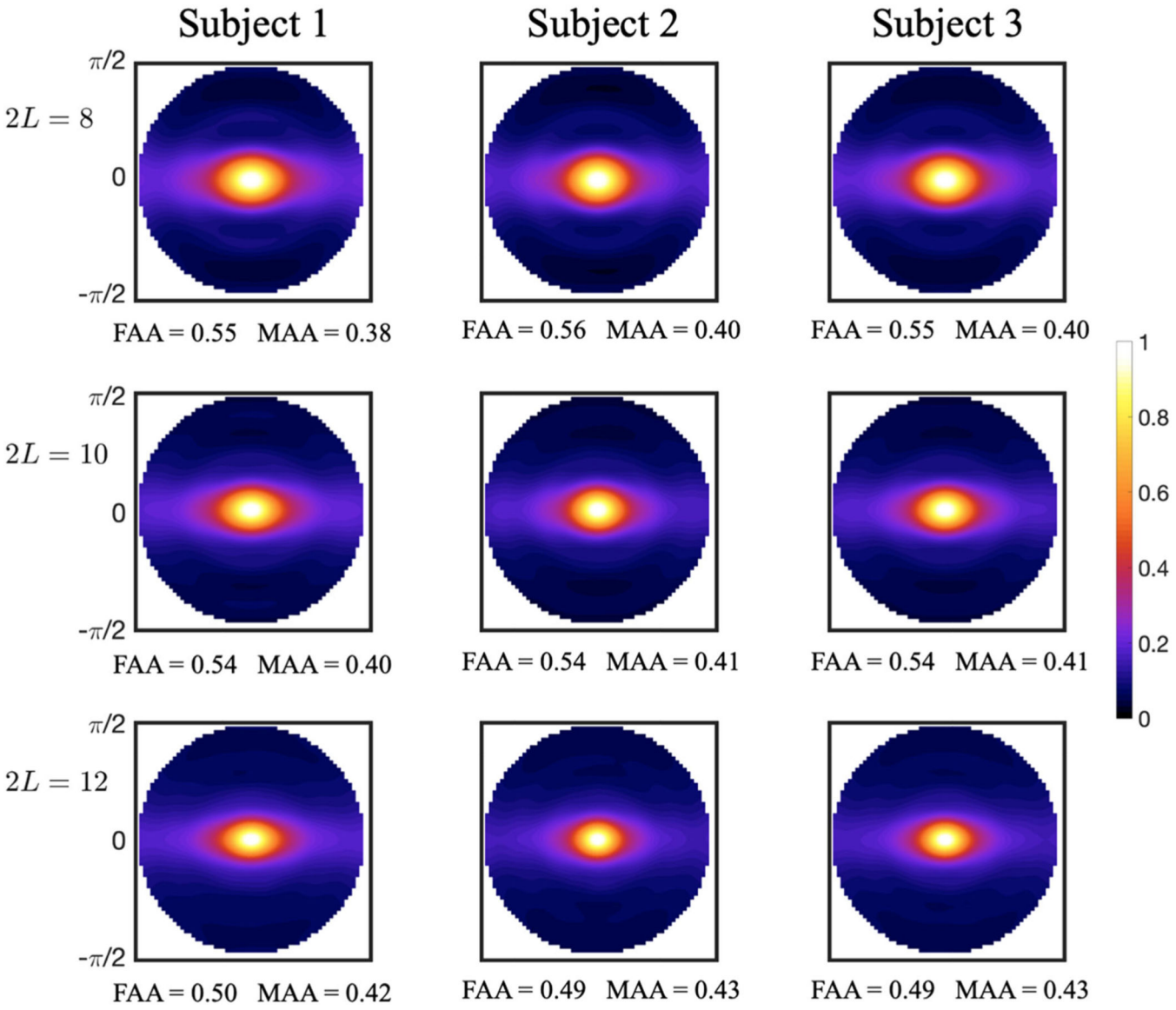

FIGURE 11.

Average of fODFs over all white matter voxels for each of three subjects. The averages are calculated using the fODFs' local frames of reference in order to remove the effect of relative spatial orientation in the laboratory frame. The *b*-value is 8000 s/mm^2, D_0 is set to D_a, and $2L$ is set to 8, 10, and 12. Note that the FAA decreases slightly with increasing $2L$ while the MAA becomes larger

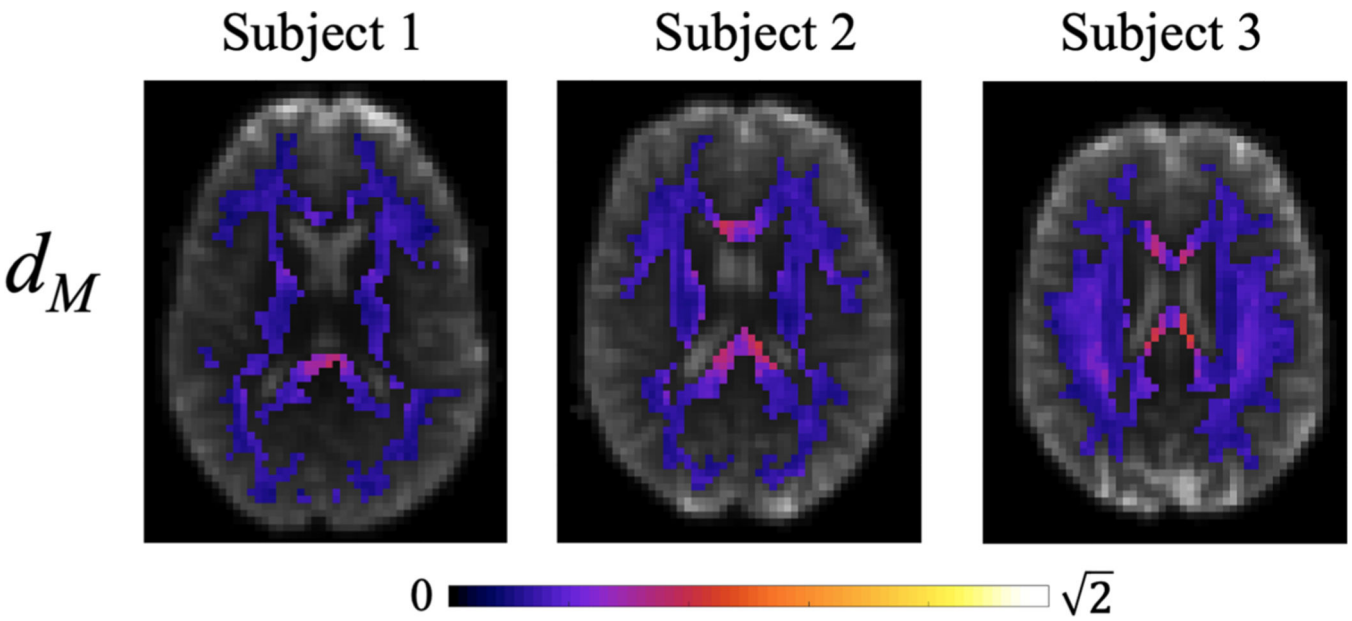

FIGURE 12.

Maps of the Matusita distance between fODFs in each white matter voxel and the average fODF for selected slices from three subjects with white matter shown in color. The *b*-value is 8000 s/mm^2, D_0 is set to D_a, and $2L$ is set to 10. The distances are for the local reference frames, with the average fODFs being determined separately for each subject using all white matter voxels from the entire cerebrum. Relatively large differences are apparent in the genu and splenium of the corpus callosum, showing that these regions have atypical fODFs

TABLE 1

Ideal angular resolution α_{2L} for the fODF represented as a spherical harmonic expansion with a maximum degree $2L$. N_{2L} is the number of terms in the expansion, which gives the minimum number of distinct diffusion encoding directions needed to uniquely determine the expansion coefficients with FBI. The calculations using Equation 12 assume $D_0 = D_a$ and correspond to the best achievable resolution for a given choice of $2L$

$2L$	N_{2L}	α_{2L} (°) (Equation 12)	α_{2L} (°) (Equation 13)
2	6	78.46	80.20
4	15	47.58	47.93
6	28	34.40	34.51
8	45	26.99	27.04
10	66	22.22	22.24
12	91	18.90	18.90
14	120	16.44	16.44
16	153	14.55	14.55
18	190	13.05	13.04
20	231	11.83	11.83

TABLE 2

Summary of the effects of altering the diffusivity scale D_0, the maximum spherical harmonic expansion degree $2L$, the number of diffusion directions N, and the diffusion weighting b. Adjusting each parameter may have both beneficial and deleterious effects. An imaging protocol and data analysis optimized for high fidelity fODFs requires careful balancing of these various factors. Beneficial effects are underlined.Recommended values are listed in parentheses and are appropriate for high fidelity fODFs on clinical 3 T scanners

Parameter	Effects of increasing	Effects of decreasing
D_0 (D_a or 3 μm^2/ms)	Smooths fODF; reduces sensitivity to signal noise and sampling errors	Increases fODF accuracy and improves angular resolution as long as $D_0 \geq D_a$; increases sensitivity to signal noise and sampling errors
$2L$ (8, 10, or 12)	Improves angular resolution; increases sensitivity to signal noise and sampling errors	Smooths fODF; reduces sensitivity to signal noise and sampling errors
N (2 to 3 times N_{2L})	Increases image acquisition time; reduces sensitivity to signal noise and sampling errors	Reduces image acquisition time; increases sensitivity to signal noise and sampling errors
b (6000 to12000 s/mm^2)	Improves fODF accuracy by suppressing dMRI signal from extra-axonal water; increases precision with which higher degree spherical harmonic coefficients can be estimated; reduces sensitivity to choice of D_0; decreases SNR; increases image acquisition time	Lowers fODF accuracy by increasing contribution to dMRI signal from extra-axonal water; decreases precision with which higher degree spherical harmonic coefficients can be estimated; increases sensitivity to choice of D_0; increases SNR; decreases image acquisition time